國立臺灣大學理學院物理學研究所

碩士論文

Department of Physics
College of Science
National Taiwan University

Master Thesis

金奈米球的非線性散射強度調節之機制

The mechanisms of amplitudinal modulation of nonlinear scattering in gold nanospheres

沈柏廷

Po-Ting Shen

指導教授：朱士維 博士

Advisor: Shi-Wei Chu, Ph.D.

中華民國 105 年 8 月

August, 2016

doi:10.6342/NTU201602833

國立臺灣大學碩士學位論文
口試委員會審定書

金奈米球的非線性散射強度調節之機制
The mechanisms of amplitudinal modulation of nonlinear scattering in gold nanospheres

本論文係 沈柏廷 君（R03222026）在國立臺灣大學物理學系、所完成之碩士學位論文，於民國 105 年 07 月 15 日承下列考試委員審查通過及口試及格，特此證明

口試委員：

朱士維 （簽名）

（指導教授）

劉祥麟　　陳國平

林宮元　　[illegible]

doi:10.6342/NTU201602833

誌謝

兩年前剛從台大數學畢業的我原本對自己的能力很沒信心，多虧朱士維老師一路的鼓勵、指導，才能讓我在碩班短短兩年內脫胎換骨，在研究上、期刊、各種會議表現亮眼，甚至得到申請理學院院長獎的機會。這些成就都是兩年前的我想都不敢想的。因此，我要特別感謝朱士維老師的用心指導，無論是在研究還是做人，朱老師都樹立了一個典範。

我也要感謝實驗室的每一位成員對我的支持與鼓勵，我最感謝的同學是冠郁和億城，常常和我討論研究上的問題，讓我受益良多。凱評和致維在的總務上的協助讓我省去不少報帳的時間。國仁和 Deka 的指導讓我的口頭報告與寫作能力大幅提升，特別是與 Deka 交談的機會，讓我的英文口說進步神速。彥達和李炫留下非常寶貴的實驗資料，讓我的工作非常順利。實驗室的學弟妹們也非常優秀，厚獻是一個稱職的聽眾，與柏萱和毓婷的合作也讓我學到很多。

最後，我要感謝我的父母，在大學四年的人生低潮中，總是激勵著我，從來沒有干涉我想做的任何事，並支持我的一切選擇。

doi:10.6342/NTU201602833

中文摘要

貴金屬奈米粒子的非線性在過去數十年當中已被廣泛地研究。由貴金屬形成的電漿子奈米粒子可以藉由它們高載子密度與獨特的價帶結構，來提升金屬中的非線性。這些奈米粒子的非線性有兩個重要應用：在生物成像中作為非線性標記，以及全光學信號控制 。最近，我們發現一種新的非線性現象，那就是當金奈米粒子受到連續波雷射激發時，會產生非線性散射。一般來說，散射是線性的，即入射光強度與散射光強度成正比。而我們發現，當金奈米粒子受到激發時，散射並不會隨著入射增加，顯示出非常強的非線性。在高激發強度下(MW/cm^2)，散射會偏離至線性趨勢以下，若繼續提高激發強度，散射反而會超過線性趨勢。我們把前者命名為「飽和散射」，後者則命名為「反飽和散射」。這新穎的非線性首先被利用在超解析顯微術，可以使電漿子奈米結構的解析度提高至八分之一波長，而在最近，被利用於全光學開關，可以使信號被關閉 80%。間接證據顯示熱晶格是「飽和散射」的主要機制，但是，信號的關閉深度、與「反飽和散射」皆無法被已知的古典模型所預估。在本篇論文裡，我們首先透過實驗驗證熱晶格主張，接著透過米氏理論，並使用溫度相關的介電系數計算孤立奈米粒子的散射光譜。我們先示範信號的非線性無法被已知的古典模型推估，並從馬克斯威-賈內理論得到提示：奈米粒子與塊材應具有不同的介電系數。於是我們修正了羅倫茲-德魯模型，加上了代表局部表面電漿振動的振子。出乎意料地，該振子的羅倫茲-德魯參數揭露了熱晶格如何參與非線性散射。這模型能夠精確描述「飽和散射」，也暗示了「反飽和散射」應該是仰賴其他的機制。

關鍵字：飽和散射、奈米金粒子、熱晶格、非線性光學、表面電漿共振

doi:10.6342/NTU201602833

ABSTRACT

Nonlinearity in noble metallic nanoparticles has been studied extensively for decades. Plasmonic nanoparticles made of noble metals enhances the nonlinearity due to their high carrier density and unique band structures. Two important applications are nonlinear labels in bio-imaging, and all-optical signal manipulations. Recently, we discovered a new nonlinear phenomenon on the scattering of gold particles when excited by continuous-wave (CW) lasers. Conventionally, scattering should be linear, i.e. proportional to the incident intensity. We found that when the excitation intensity in gold nanospheres increases, the scattering may not increase accordingly, showing significant nonlinear response. At high intensity (MW/cm^2), the scattering is below the linear trend, and if the intensity further increases, the scattering surpasses the linear trend. We describe the former as "saturable scattering" and the latter as "reverse saturable scattering." The novel nonlinearity has been first applied to super-resolution microscopy with spatial resolution of plasmonic nanostructures down to $\lambda/8$, and recently used in ultrasmall all-optical switching with up to 80% modulation depth. The mechanism of saturable scattering has been proposed with indirect evidence: hot lattice is the major mechanism. Nevertheless, the modulation in scattering amplitude cannot be calculated through known classical models, and the mechanism for reverse saturable scattering is still unknown. In this work, we first confirm the proposition for hot lattice with experiments, then calculate the single-particle scattering spectrum with temperature-dependent permittivity by Mie theory. We compare the calculation to experiments to show the nonlinearity cannot be obtained through known classical models, then derive hints from Maxwell-Garnett theory. From the hints, we propose that nanoparticles having different permittivity to that of the bulk material. Thus, we correct the Lorentz-Drude model with an oscillator representing

doi:10.6342/NTU201602833

the localized surface plasmon. Surprisingly, the Lorentz-Drude parameters of such oscillator unveil how hot lattice participate in nonlinear scattering. The model provides accurate description for saturable scattering. It also implies the reverse saturable scattering should rely on other mechanisms.

Keywords: saturable scattering, gold nanoparticles, hot lattice, nonlinear optics, surface plasmon resonance

doi:10.6342/NTU201602833

CONTENTS

口試委員會審定書 ..... #

誌謝 i

中文摘要 ii

ABSTRACT iii

CONTENTS v

LIST OF FIGURES viii

LIST OF TABLES xi

Chapter 1 Overview 1

1.1 Plasmons and optical nonlinearity 1

1.2 Saturable scattering and reverse saturable scattering in noble metallic nanoparticles 3

1.3 Unusually deep modulation of saturable scattering 4

1.4 Goal and outline 6

Chapter 2 Principles 7

2.1 Localized surface plasmon resonance 7

2.2 The mechanism of saturable scattering and nonlinear refractive indices 7

2.3 Lorentz-Drude model and dielectric function of metal 12

2.3.1 Lorentz-Drude model [43] 12

2.3.2 Temperature-dependence of the Lorentz-Drude parameters 15

2.4 Mie theory 15

2.5 Maxwell-Garnett theory 16

2.5.1 Conventional Maxwell-Garnett theory 16

doi:10.6342/NTU201602833

2.5.2 Adaptation of Maxwell-Garnett theory on single-particle 18
2.5.3 The contribution of ambient medium 20
2.6 Hints from Maxwell-Garnett theory 21
Chapter 3 Experiments 23
3.1 Sample preparation 23
3.1.1 Gold nanospheres 23
3.1.2 Bulk gold 23
3.1.3 Immersion oil 23
3.2 Experiment setup 24
3.2.1 Confocal microscope equipped with spectral detection for single-particle experiments 24
3.2.2 Temperature-dependent ellipsometry 29
3.2.3 Abbe refractometer 29
3.3 Experiment results 29
3.3.1 Intensity dependence of single-particle nonlinear scattering 29
3.3.2 Single-particle scattering modulation by CW 30
3.3.3 Single-particle scattering modulation by environmental heating 31
3.3.4 Temperature-dependent bulk gold permittivity 33
3.3.5 Temperature-dependent immersion oil refractive index 37
3.4 Discussion 38
Chapter 4 Permittivity of single particle 40
4.1 Conventional Mie theory 40
4.2 Single-particle permittivity based on the hints from Maxwell-Garnett theory 41
4.3 Model of single-particle permittivity: with damping of LSP 44

doi:10.6342/NTU201602833

4.4 Discussion.....49

4.4.1 The applicability of the LSP damping model and further developments.....49

4.4.2 Possible mechanism for reverse saturable scattering.....50

Chapter 5 Conclusion 52

REFERENCE 53

doi:10.6342/NTU201602833

LIST OF FIGURES

Figure 1. The comparison of thermoreflectance of gold nanoparticles (diameter 5nm) and bulk gold (As defined in (9), p=0.08). Replotted from [47]. 18

Figure 2. Calculation of Maxwell-Garnet formula with different volume fraction (a) p=0.08 and (b) p=0.3; Assume the temperature dependence of the ambient medium to be $d_T n_{med}$=-3×10^{-4} K^{-1}; Temperature-dependence extracted from our measurement.....20

Figure 3. Calculation of Maxwell-Garnet formula with different volume fraction (a) p=0.08 and (b) p=0.3. Assume the temperature dependence of the ambient medium to be $d_T n_{med}$ =0 21

Figure 4. (a) Experimental setup, consisting of a confocal microscope, a hot plate on the microscope, a supercontinuum (WL-SC-400-2, Fianium Ltd.) with 200ps output pulsed width, a spectrometer (Shamrock 163 with iDus Cameras DV420A-OE, Andor Technology), and a PMT (H5783-01, Hamamatsu). The confocal microscope is composed of a custom galvo scanning system, upright microscope (BX-53, Olympus), and a 100x objective. (b) Image of single-particles under confocal microscope. Field of view: 25μm×25μm 24

Figure 5. The (a) single-particle backscattering (b) reflection from the substrate of an isolated particle. (c) The reference of the supercontinuum source. (d) The single particle scattering determined by [(a)-(b)]/(c). Replotted from [50]..26

Figure 6. The confocal image of (a) 300K (b) 325K. The center is marked by the text "μm". The white triangles marks the nanoparticles being tracked. Field of view: 50μm×50μm.....27

Figure 7. The (a) single-particle backscattering (b) reflection from the substrate of an

doi:10.6342/NTU201602833

isolated gold nanosphere (80nm as diameter) at different temperatures. 28

Figure 8. Intensity dependence of nonlinear scattering by 561-nm CW laser. Red dots are the scattering intensity of the laser. At low intensity, the red dots form a linear relationship, as shown by the blue dashed line. On the other hand, the nonlinear scattering curve (green line) and the corresponding n_2 is determined by fitting the red dots with equation (16). 30

Figure 9. As the excitation intensity of 561nm CW laser increases, the scattering intensity of supercontinuum decreases. The blank of the spectrum is due to the notch filter that protects the spectrometer from excess 561nm laser.....31

Figure 10. Heating the gold nanospheres by a hot plate to induce significant scattering variation. (a) Statistics on the scattering intensity of 80nm-diameter gold nanosphere at different temperatures. Thick-solid line: averaged scattering intensity; Thin-light line: raw data. (b) Tracking the same 60nm-diameter gold nanosphere with finer temperature resolution. 33

Figure 11. (a) The real part ε' and (b) imaginary part ε" of permittivity of gold at room temperature. Morphology (c) before annealing (d) after annealing. Scale bar: 400nm. Replotted from [33]. 34

Figure 12. The real part ε' and (b) imaginary part ε" of permittivity with unannealed gold films in the visible band. (c) and (d) are the thermo-derivatives of ε' and ε". 35

Figure 13. (a) The real part ε' and (b) imaginary part ε" of permittivity with annealed gold films in the visible band. (c) and (d) are the corresponding thermo-derivatives of ε' and ε". 37

Figure 14. Temperature dependence of oil index. 38

Figure 15. Calculated Mie scattering efficiency of 80nm gold nanosphere. Permittivity

doi:10.6342/NTU201602833

from (a) unannealed (b) annealed gold film. The temperature-dependent refractive index of ambient medium is extracted from 3.3.5.....41

Figure 16. The calculated scattering modulation of 80nm gold nanosphere based on the hints from Maxwell-Garnett theory. Empirical parameters are A_1=1, A_2=7, Δn_{med} =-0.02 for 350K; A_1=3, A_2=14, Δn_{med} =-0.0365 for 400K 42

Figure 17. The calculated scattering modulation of 80nm gold nanosphere based on the hints from Maxwell-Garnett theory. Empirical parameters for the red curve are A_1=3, A_2=14, Δn_{med} =-0.0365 for 400K; for the blue curve A_1=3, A_2=14, Δn_{med} =0 43

Figure 18. The effective permittivity derived from the hints of Maxwell-Garnett theory. 44

Figure 19. (a) The real part ε' and (b) imaginary part ε" of permittivity calculated by Lorentz-Drude model without LSP damping. (c) The calculated Mie scattering efficiency from (a) and (b). 48

Figure 20. (a) The real part ε' and (b) imaginary part ε" of permittivity calculated by Lorentz-Drude model with LSP damping. (c) The calculated Mie scattering efficiency from (a) and (b).....49

doi:10.6342/NTU201602833

LIST OF TABLES

Table 1 Demonstration of newly defined p. Each p is linked to a specific particle diameter and a respective resonance.....19

Table 2 Nonlinear refractive indices and temporal scale. Listed in 2.2.....39

Table 3 The room temperature fitting parameters of Lorentz-Drude model [56], and possible LSP parameters.....45

Table 4 The fitting parameters of LSP damping in Figure 20. 49

doi:10.6342/NTU201602833

Chapter 1 Overview

1.1 Plasmons and optical nonlinearity

Plasmon is a quantum (minimal quantity involved in a physical interaction) of plasma oscillation (rapid oscillation of electron density in media), just like the photons and phonons are quanta to light and lattice vibration respectively. The concept was first proposed by David Pines and David Bohm in 1952 [1]. The idea was started as a single spark but turned into a prairie fire. Light and a material interact with each other through the coupling of photons and plasmons. For the light frequency below the plasma frequency, it will be reflected (shielding effect). For the light frequency above the plasma frequency, the light is transmitted. For most metals, the plasma frequencies are located in ultraviolet regime, so they are reflective to the visible light. In some noble metals, there are interband transitions in the visible band. These interband transitions absorb visible light and give noble metals gorgeous colors.

The surface plasmons (SP) are the plasmons confined to the interface of a material and surrounding medium. When SPs couples with photons, they form polaritions (bosonic quasiparticles). We call such coupling as surface plasmon polaritons (SPP). The SPPs strengthen the electromagnetic field around the interface. When the surface plasmons are confined to a nanostructure, they become localized surface plasmons (LSP) and significantly increase the electromagnetic field localized to the surrounding of the nanostructure. The electromagnetic field falls off a short distance away from the nanostructure.

Typically, in light-matter interactions (absorption, scattering, or fluorescence), the radiated intensity is proportional to the incident intensity [2]. The optical nonlinear process occurs when the optical fields of incident light is strong enough to produce

doi:10.6342/NTU201602833

polarization fields proportional to the quadratic, cubic or higher power of the incident fields in a material. Since both SPP and LSP enhance the local electromagnetic fields, the optical nonlinearities are significantly amplified [3]. These plasmonic excitations boost the optical nonlinearities in two ways [3, 4]:

1. The strong electromagnetic fields in SPs enhance the instantaneous optical process (whose timescale is only a few femtoseconds), e.g. surface-enhanced Raman scattering. This equates to higher effective optical nonlinearity, and allows ultrafast all-optical signal modulations.

2. SPs are very sensitive to the surface and surrounding they propagate on. Small alteration to the media significantly changes the surface plasmon resonances (SPR). SPPs can be used as biosensors, and LSP are particularly useful as nonlinear labels in bio-imaging [5].

A specific branch called nanoplasmonics is dedicated to the application of SPs in nanostructures made of plasmonic materials. The most popular materials are noble metallic nanoparticles. The nonlinearities in these nanoparticles has been studied for decades.

In the early studies, the noble metallic nanoparticles are excited by pulsed lasers, such as [6, 7]. The interesting nonlinear interactions of electrons and phonons due to the non-equilibrium state of electron temperature and lattice temperature are extensively studied. Later, the thermal equilibrium state of electron and lattice temperature draws great interests. The nanoparticles are either heated with continuous-wave (CW) lasers [8, 9], or environmental heating [10, 11]. The dedicated topic about thermally excitation on nanostructures is referred to as thermo-plasmonics [9, 12].

With the capability of nanoscaled heat generation, thermo-plasmonincs has a wide range of applications: photothermal imaging [13], cancer treatment [14], super-resolution

doi:10.6342/NTU201602833

microscopy [13, 15, 16], plasmonic photovoltaics [17], and water boiling, sanitation and super-heating [18-20], up to thermo-photovoltaics [17], solar thermo-electric generators [21], plasmon-mediated photocatalysis [22], plasmon-assisted chemical vapor deposition [23] and heat-assisted magnetic recording [24]. Therefore, it is crucial to study the optical nonlinearities induced by equilibrium state dynamics of plasmonic nanostructures.

1.2 Saturable scattering and reverse saturable scattering in noble metallic nanoparticles

Recently, we discovered a new nonlinear phenomenon on the scattering of gold particles when excited by CW lasers. Conventionally, scattering should be linear, i.e. proportional to the incident intensity. We found that when the excitation intensity in gold nanospheres increases, the scattering may not increase accordingly, showing significant nonlinear response [25, 26]. Below 1 MW/cm^2, the scattering is linear to the incident intensity. However, around 1 MW/cm^2, the scattering deviates below the linear trend and, above 1 MW/cm^2, exceeds the linear trend. We describe the former as "saturable scattering" and the latter as "reverse saturable scattering."

The novel nonlinearity has been first applied to super-resolution microscopy with spatial resolution of plasmonic nanostructures down to $\lambda/8$ [25], and recently used in ultrasmall all-optical switching [27] with 90% modulation depth. The emergent applications made use of the strengths of nonlinear scattering: nanoscale, ultrafast, low operating power, broad-band, and high switching modulation depths.

Although the nonlinearity has so many potential applications, the mechanism is unclear. In Huang's thesis [28], the mechanism of nonlinear scattering is proposed to be highly related to the third order nonlinearity of noble metals, and localized surface plasmon resonance (LSPR). There are several third order nonlinear mechanisms, including

doi:10.6342/NTU201602833

intraband transition, interband transition, hot electron, and hot lattice. Huang found indirect evidence to show that the rising of lattice temperature (hot lattice) should be the most possible mechanism. However, to confirm the proposition, more solid evidence should be provided. For each nonlinear mechanism, there's a respective n_2, whose quantity is positively correlated to the temporal response of light-matter interactions. The time scale of excitation should be a solid evidence to verify the mechanism. Therefore, in 3.4, the effective nonlinear refractive index (n_2) of nonlinear scattering will be carefully examined.

1.3 Unusually deep modulation of saturable scattering

One of the unusual properties of saturable scattering is the deep modulation, which is up to 90% of the scattering amplitude off, as demonstrated by switching the off-resonance wavelength with on-resonance wavelength [27]. In the literature, several temperature-dependent studies have been made [10, 29]. The reported highest temperature studied is up to 1200K [10]. However, the modulation depths (optical extinction compared to 300K) of the absorption spectra of gold nanospheres at 400K (embedded in silica) is less than 20%, which is very different from what we observed in the hot plate experiment (At 400K, we experimentally achieved 70% modulation depths.) The reason is that Yeshchenko *et al* [10] and other conventional studies traced back to El-Sayed [29] only measure the matrix absorption spectra. Since more than 90% of the light is from transmission of the host medium, the actual single-particle modulation depth cannot be evaluated.

Since their modulation depths cannot be compared to ours, we looked for the temperature-dependent permittivity of bulk gold to calculate nonlinear scattering of gold nanospheres. In general, the imaginary part of the permittivity is theoretically account for the modulation depths of nanoparticles. Surprisingly, the experimental measurements of

doi:10.6342/NTU201602833

the temperature dependence of the permittivity of various metals are so scarce that no complete and correlated set of data for the complex metal permittivity as a function of temperature from room temperature up to the melting temperature was reported. Therefore, we measure the temperature dependence of gold permittivity with fine temperature resolution. We also find that the crystallographic structure of the film has an obvious influence on the temperature variation of the gold film. In the visible band, the unannealed gold has almost twice the variation of annealed gold in imaginary part of permittivity. We also notice a commonly ignored concept in thermo-plasmonic studies: most studies used permittivity from annealed metal, while most metallic nanoparticles are fabricated in chemical solutions[30], they are in nature multi-crystalline, i.e. unannealed. It is apparently critical to consider the crystallographic factor for plasmonic calculations.

In addition to the permittivity of gold, Mansour and Sarkhosh [8] pointed out the nonlinearity from the ambient medium to be equally important. The nonlinear refractive index of gold nanoparticle colloids is significantly affected by thermal conductivity of the ambient medium. The lower the thermal conductivity, the larger the n_2 induced by CW laser. More interestingly, the n_2 of nanoparticles in castor oil, which should resemble our testing environment (immersion oil), is 19 times the n_2 of nanoparticles in water. Hence, the ambient medium could be another important contributor to the modulation depth. Besides, we should consider the temperature dependence of the ambient medium. The complex refractive index ($\tilde{n} = n + i\kappa$) changes with temperature in most oils, but the majority of the change is in the real part [31, 32]. The reported thermo-derivative of refractive index for the real part ($d_T n$) is about 10^{-4}, and 10^{-7} for the imaginary part ($d_T \kappa$)[31]. For system with negligible absorption, n_2 is solely linked with n. It is unlikely that the temperature dependence of the κ make a difference to the thermal modulation

doi:10.6342/NTU201602833

depths. That is, for the ambient medium, the real thermo-derivative of the refractive index ($d_T n$) should be responsible for part of the modulation depths.

1.4 Goal and outline

Nonlinear scattering in plasmonic nanoparticles has been shown to have great potential in applied physics, and thermo-plasmonics. However, the mechanism of saturable scattering was not confirmed. In this work, we first provide strong evidence to Huang's proposition on the hot lattice [28]. Next, we calculate the single-particle scattering spectrum based on experimental data of bulk gold [33] and ambient medium by Mie theory and compare the results to experiments. In the beginning, the modulation depths is much less than our experimental observation. We show the modulation depths cannot be obtained through known conventional Mie theory, then propose our own model that can explain the unusually deep modulation depths of nanoparticles [27].

In Chapter 2, we list all the formulas and theory that we will use to determine the mechanism of saturable scattering and calculate the modulation depths. In Chapter 3, we measure the intensity-dependent refractive index of nonlinear scattering, the temperature-dependent spectroscopic information of nonlinear scattering, and the temperature-dependent permittivity of gold and immersion oil for later calculations. At the end of the chapter, we conduct detailed comparison on the nonlinear refractive indices (n_2) to verify the mechanism to be hot lattice. In Chapter 4, we modify the dielectric function for single-particle and calculate the resulted scattering intensity. With such modification, we generate enough modulation depths. We then discuss the model. Chapter 5 is the conclusion.

doi:10.6342/NTU201602833

Chapter 2 Principles

2.1 Localized surface plasmon resonance

Surface plasmon (SP) is an oscillation of coherent electrons due to the change of sign at the interface of positive and negative permittivity medium. The oscillating frequency of such oscillation is called the surface plasmon resonance (SPR). When the interface is limited to a microstructure, the field strength is significantly increased, and so is the nonlinearity of the embedded material. This special case of SP is named as localized surface plasmon resonance (LSPR). One can solve the Maxwell equations at the interface of sphere and ambient medium by analytic Mie theory [34] to obtain the scattering and absorption of the sphere. The resonance of metallic nanospheres can very broad, ranging from ultraviolet to infrared. In the case of gold nanosphere, the resonance is in the visible band (390-780nm), depending on the particle size and refractive index of the ambient medium.

2.2 The mechanism of saturable scattering and nonlinear refractive indices

We begin with the mathematical tools to describe nonlinear scattering. In nonlinear optics, the refractive index of many materials as

$$n = n_0 + \bar{n}_2 \left\langle \bar{E}^2(t) \right\rangle , \tag{1}$$

where the bracket represents time average [35]. n_0 is the usual weak-field refractive index, and the $\bar{n}_2$ is a new optical constant influenced under high optical intensity. If the optical field can be written as

doi:10.6342/NTU201602833

$$\vec{E}(t) = E(\omega)e^{-i\omega t} \ , \tag{2}$$

then

$$\left\langle \vec{E}^2(t) \right\rangle = 2E(\omega)E(\omega)^* = 2\left|E(\omega)\right|^2 , \tag{3}$$

We find that

$$n = n_0 + 2\bar{n}_2\left|E(\omega)\right|^2 \equiv n_0 + n_2 I \ , \tag{4}$$

where

$$I = 2n_0\varepsilon_0 c\left|E(\omega)\right|^2 \tag{5}$$

is the time average laser power, and n_2 is the newly defined nonlinear refractive index.

In general, the optical nonlinearity can written as the polarization $\vec{P}(t)$ as a power series of field strength $\vec{E}(t)$ [36]

$$\vec{P}(t) = \varepsilon_0[\chi^{(1)}\vec{E}(t) + \chi^{(2)}(t)\vec{E}(t)\vec{E}(t) + \chi^{(3)}\vec{E}(t)\vec{E}(t)\vec{E}(t)] \ , \tag{6}$$

where t is the time, and $\chi^{(k)}$ is the k_{th} order susceptibility.

The first order, of course, is the linear susceptibility. We refer the second order nonlinear polarization as

$$\vec{P}_2(t) = \varepsilon_0\chi^{(2)}(t)\vec{E}(t)\vec{E}(t) \ , \tag{7}$$

and the third order nonlinear polarization as

$$\vec{P}_3(t) = \varepsilon_0\chi^{(3)}\vec{E}(t)\vec{E}(t)\vec{E}(t) \ . \tag{8}$$

Typically, the second order nonlinearity vanishes for a centrosymmetric material (e.g. gold, if the structure is not processed on purpose). For simplicity, we assume the incident light is linearly polarized, and the suppressing the $\chi^{(3)}$. Also, in the case of CW laser,

doi:10.6342/NTU201602833

the time-oscillating term of the electric field can be ignored. The nonlinear polarization is thus written as

$$P_{NL}(\omega) = 3\varepsilon_0 \chi^{(3)} \mid E(\omega) \mid^2 \; E(\omega) \; , \tag{9}$$

and the total polarization of the material is

$$P^{TOT}(\omega) = \varepsilon_0 [\chi^{(1)} + 3\chi^{(3)} \mid E(\omega) \mid^2] E(\omega) \equiv \varepsilon_0 \chi_{eff} E(\omega) \; . \tag{10}$$

where we introduced the effective susceptibility

$$\chi_{eff} \; = \chi^{(1)} + 3\chi^{(3)} \mid E(\omega) \mid^2 \; . \tag{11}$$

In order to relate the nonlinear susceptibility $\chi^{(3)}$ to nonlinear refractive index n_2, note that it is generally true that

$$n^2 = 1 + \chi_{eff} \; . \tag{12}$$

Therefore, from (4), (11), and (12)

$$(n_0 + n_2 I)^2 = 1 + \chi^{(1)} + 3\chi^{(3)} \mid E(\omega) \mid^2 \; . \tag{13}$$

By expanding the quadratic, we finally have

$$n_0 = (1 + \chi^{(1)})^{1/2} \; , \tag{14}$$

and

$$n_2 = \tfrac{3}{4 n_0{}^2 \varepsilon_0 c} \chi^{(3)} \; . \tag{15}$$

In the range of LSPR, there are four possible candidates for the nonlinear scattering of gold nanospheres, including intraband transition, interband transition, hot electron, and hot lattice. They are all related to third order nonlinearity ($\chi^{(3)}$) of noble metals and each of them has an effective nonlinear refractive index (n_2), which can be found in the

doi:10.6342/NTU201602833

literature. To simplify the comparison, we converted reported $\chi^{(3)}$ to n_2 with (15). Please note that nonlinear index can be significantly affected by the temporal response of the corresponding light-matter interactions, so it is crucial to check the time scale of excitation [37]. For example, the first two mechanisms are intraband and interband transitions. The former is the transition between quantized levels within conduction or valence band in a few femtoseconds, and the latter is the transitions between conduction and valenceband in tens of femtoseconds. One classical example of nonlinear optical interaction that is related to these two transitions is four-wave mixing, from which the reported n_2 corresponding to intraband transition sits below $10^{-12} cm^2/W$, and the n_2 corresponding to interband transition ranges from $10^{-12} \sim 10^{-10} cm^2/W$ [38]. On the other hand, hot electron represents the thermalization of conduction electron above Fermi surface in less than a picosecond. The extensively studied nonlinear optical example for hot electron is the optical Kerr effect, from which the corresponding n_2 is estimated in the range of $10^{-10} \sim 10^{-8} cm^2/W$ [39]. For timescale extending from picosecond to nanosecond, the thermal energy shall be transferred from electron to lattice, resulting in hot lattice. This mechanism is generally ignored in previous pump-probe experiments based on femtosecond excitations. However, when using nanosecond excitation or even CW excitation, the corresponding n_2 reaches $10^{-8} cm^2/W$ or even larger [8, 39]. The comparison of the above mechanisms can be found in Table 2.

In addition to the third order nonlinearity of the metal, the nonlinearity from the ambient medium should be also examined. The reported n_2 of organic materials itself is much smaller than plasmonic metals [39-41]. For example, under CW excitation, the n_2 of olive oil is $10^{-8} cm^2/W$, while the n_2 of gold is at least one order larger. Hence, the third order nonlinearity from the ambient medium is insignificant in our case.

doi:10.6342/NTU201602833

With this order of magnitude knowledge, we then extract corresponding nonlinear index from our single-particle nonlinear scattering measurement. The first experiment is to measure the scattering intensity dependency of the 561-nm CW laser from isolated gold nanospheres. Our previous work suggests that nonlinear scattering intensity dependence is a polynomial function, which implicitly contains the nonlinear refractive index [42]. By fitting the nonlinear scattering curve, we can derive both the first and second order coefficients to obtain the corresponding nonlinear refractive index (n_2), as outlined in the following.

By assuming that the scattering signal comes from the real part index mismatch Δn between the metallic nanoparticle and the surrounding medium. The nonlinear scattering curve can be described as following:

$$S(I) = \alpha_{s_0} I + \gamma_s I^2, \tag{16}$$

,where from Rayleigh-Gans formalism

$$\alpha_{s_0} = g_s (\Delta n_L)^2 , \tag{17}$$

and

$$\gamma_s = 2 g_s \Delta n_L \Delta n_2 . \tag{18}$$

Here g_s is an intensity-independent parameter depending only on size of the particle. Δn_L is the linear refractive index difference of the host medium (immersion oil, n=1.518, Olympus) and gold. Δn_2 is the nonlinear refractive index difference of the host medium and metallic nanosphere. In our case, the host medium is assumed to have no nonlinearity. Therefore, Δn_2 is the n_2 of gold.

From (17) and (18), we have

doi:10.6342/NTU201602833

$$\Delta n_2 = \frac{\Delta n_L}{2} \frac{\gamma_s}{\alpha_{s_0}} \ . \tag{19}$$

2.3 Lorentz-Drude model and dielectric function of metal

2.3.1 Lorentz-Drude model [43]

In typical Drude model, the movement of conduction electrons in metals (ions) can be described as the equation of motion of springs:

$$m\frac{\partial^2 \vec{r}}{\partial t^2} + m\Gamma\frac{\partial \vec{r}}{\partial t} + m\omega_0{}^2\vec{r} = -q\vec{E} \qquad , \tag{20}$$

where m should be interpreted as effective electron mass m_e, Γ is the damping rate, and ω_0 is the frequency of restoring force.

After Fourier transform, the equation becomes

$$m(-j\omega)^2\vec{r}(\omega) + m(-j\omega)\vec{r}(\omega) + m\omega_0{}^2\vec{r}(\omega) = -q\vec{E} \ . \tag{21}$$

Hence, the displacement of conduction electrons to the ions is

$$\vec{r}(\omega) = -\frac{q}{m_e}\frac{\vec{E}(\omega)}{\omega^2{}_0 - \omega^2 - j\omega\Gamma} \ . \tag{22}$$

The dipole moment of electrons is thus

$$\vec{\mu}(\omega) = -q\vec{r}(\omega) \ . \tag{23}$$

The Lorentz polarizability $\alpha(\omega)$ is defined as

$$\vec{\mu}(\omega) = \alpha(\omega)\vec{E}(\omega) \ . \tag{24}$$

where

$$\alpha(\omega) = \frac{q^2}{m_e}\frac{1}{\omega^2{}_0 - \omega^2 - j\omega\Gamma} \ . \tag{25}$$

represents the polarizability of a single atom.

doi:10.6342/NTU201602833

The randomness of atom forced us to take statistical average to evaluate the total polarization

$$\vec{P}(\omega) = N\langle \vec{\mu}(\omega) \rangle . \tag{26}$$

Note the definition of polarization is as followed

$$\vec{P}(\omega) = \varepsilon_0 \chi(\omega) \vec{E}(\omega) . \tag{27}$$

From (24) to (27), the susceptibility of typical Drude model

$$\chi(\omega) = \frac{{\omega_p}^2}{\omega^2{}_0 - \omega^2 + i\omega\Gamma_D} , \tag{28}$$

where the plasma frequency ω_p can be expressed as

$${\omega_p}^2 = \frac{Nq^2}{\varepsilon_0 m_e} . \tag{29}$$

Here N is now interpreted as electron density N_e.

Recall that

$$\vec{D} = \varepsilon_0 \tilde{\varepsilon}_r \vec{E} = \varepsilon_0 \vec{E} + \vec{P} = \varepsilon_0 \vec{E} + \varepsilon_0 \chi \vec{E} = \varepsilon_0 (1+\chi) \vec{E} . \tag{30}$$

Thus,

$$\tilde{\varepsilon}_r(\omega) = 1 + \chi(\omega) . \tag{31}$$

In the case of metal, the electrons move freely, so the frequency of restoring force ω_0 is zero. Hence Drude dielectric function for metal is

$$\tilde{\varepsilon}_r(\omega) = 1 - \frac{{\omega_p}^2}{\omega^2 + i\omega\Gamma_D} . \tag{32}$$

The damping frequency Γ_D can be given a more physical meaning as

doi:10.6342/NTU201602833

$$\Gamma_D = \frac{1}{\tau_D}, \tag{33}$$

τ_D is the mean collision rate of electrons, which is linked to intraband transition. Moreover, Γ_D gives the bandwidth of the damping, which is an important parameters in plasmonic studies [7].

It is worth noting in the case of nanoparticle that there's a common correction on Γ_D such that

$$\Gamma_D = \Gamma_D^{bulk} + A\frac{v_F}{R}, \tag{34}$$

where v_F is the Fermi velocity, and *R* is the radius of the particle [44]. *A* is theory-dependent parameters. In particles with *R* smaller than 10nm, *A* increases as *R* reduces due to electron-surface scattering, which is insignificant on way larger nanoparticles ($\frac{v_F}{R}$ is two order smaller than Γ_D^{bulk}; *A* is zero order). In particles with *R* smaller than 10nm, *A* increases as *R* increases due to diffusion, which is counted as extrinsic effect. Nevertheless, the plasma frequency is at the far infrared. Extending the bandwidth of damping has little effect on the visible band. Thus, we ignored (34).

However, in the real world, there are several resonances in metal due to band structures. A better approximation was provided by H.A. Lorentz in 1905.

The Lorentz-Drude model is written as

$$\tilde{\varepsilon}_r(\omega) = \tilde{\varepsilon}_r(\infty) + \omega_p^{\,2}\sum_{m=1}^{M}\frac{f_m}{\omega_{0,m}^{\,2} - \omega^2 - i\omega\Gamma_m}, \tag{35}$$

where f_m is the oscillator strength of the *m*th resonator, $\omega_{0,m}$ is the natural frequency of the *m*th resonator, and Γ_m is the damping rate of the *m*th resonator. Note that $\tilde{\varepsilon}_r(\infty)$ is for producing offset at frequencies way higher than the concerned frequencies. In

doi:10.6342/NTU201602833

general, a 5-resonator approximation provides accurate numerical values of noble metal permittivity.

2.3.2 Temperature-dependence of the Lorentz-Drude parameters

For typical Drude model, the temperature-dependence can be obtained by differentiation

$$\frac{d\omega_p}{dT} = \omega^2 \frac{\left(\frac{\Gamma_D{}^2}{\omega^2} - 1\right)\frac{\partial \varepsilon_1}{\partial T} + 2\frac{\Gamma_D}{\omega}\frac{\partial \varepsilon_2}{\partial T}}{2\omega_p}, \tag{36}$$

and

$$\frac{d\Gamma_D}{dT} = \omega^3 \frac{1 + \Gamma_D{}^2 / \omega^2}{\omega_p{}^2}\left(\frac{\Gamma_D}{\omega}\frac{\partial \varepsilon_1}{\partial T} + \frac{\partial \varepsilon_2}{\partial T}\right). \tag{37}$$

Since $\Gamma_D << \omega$, both differentiation can be approximated as

$$\frac{d\omega_p}{dT} \approx -\frac{\omega^2}{2\omega_p}\frac{\partial \varepsilon_1}{\partial T}, \tag{38}$$

and

$$\frac{d\Gamma_D}{dT} \approx \frac{\omega^3}{\omega_p{}^2}\frac{\partial \varepsilon_2}{\partial T}. \tag{39}$$

Therefore, the relative change of ω_p and Γ_D can be evaluated through temperature-dependent measurement on permittivity.

In Lorentz-Drude model, there's an additional parameter f_m to be considered. There's no simple formulation on the oscillator strength besides using quantum mechanics. However, phenomenologically, the oscillator strength increase monotonically with the temperature [45].

2.4 Mie theory

We use analytic Mie theory to calculate the scattering modulation depths[46]. The

doi:10.6342/NTU201602833

expression for Mie scattering efficiency is [34]

$$Q_{sca} = 8k^4 r^4 \left| \frac{\tilde{\varepsilon} - \varepsilon_{med}}{\tilde{\varepsilon} + 2\varepsilon_{med}} \right|^2 , \tag{40}$$

where k is the wave vector, r is the radius of particle, $\tilde{\varepsilon}$ is the permittivity of the nanosphere, ε_{med} is the permittivity of the ambient medium. The details on how to obtain the wavevector k was given by Bohren and Huffman's work [34]. It is also worth noting that Gustav Mie used bulk permittivity in his calculation, which is questionable [7].

More importantly, the resonance and amplitude of the Mie scattering comes from the term

$$f = \frac{\tilde{\varepsilon} - \varepsilon_{med}}{\tilde{\varepsilon} + 2\varepsilon_{med}} . \tag{41}$$

Our idea is that the change of permittivity ($\Delta\tilde{\varepsilon}$) of the bulk gold due to hot lattice should be carried over to the change of scattering efficiency (ΔQ_{sca}) of the gold nanosphere trough Mie theory, where

$$\Delta\tilde{\varepsilon} = \tilde{\varepsilon}(T) - \tilde{\varepsilon}(T_0) , \tag{42}$$

and

$$\Delta Q_{sca} = Q_{sca}(T) - Q_{sca}(T_0) . \tag{43}$$

2.5 Maxwell-Garnett theory

2.5.1 Conventional Maxwell-Garnett theory

Naively, one can describe the thermo-optical coefficient of metal in ambient medium as

doi:10.6342/NTU201602833

$$d_T n' = p d_T \tilde{n} + (1-p) d_T n_{med} \,, \tag{44}$$

Where p is the volume fraction of the metal, n is the complex refractive index of the metal, and n_{med} is the refractive index of the ambient medium. This approximation is oversimplified because of the lack of dielectric confinement in the nanoparticles. The change of sign of permittivity at the boundary is what gives the resonance to the metallic particle.

In general, the permittivity of inhomogeneous medium consisted of spheres in ambient medium can be well described by Maxwell-Garnett theory with the volume fraction of inclusion less than 15%. The effective permittivity is written as

$$\tilde{\varepsilon}_{eff} = \varepsilon_m \frac{\tilde{\varepsilon}(1+2p) + \varepsilon_m (1-p)}{\tilde{\varepsilon}(1-p) + \varepsilon_m (2+p)} \,, \tag{45}$$

where $\tilde{\varepsilon}$ is the complex permittivity of the metal, ε_m is the permittivity of the ambient medium, and p is the volume fraction. With sufficient conditions, the Maxwell-Garnet formula gives the value of effective permittivity at any temperature. Thus, one can derive $d_T \tilde{n}_{eff}$ through the relation

$$d_T \tilde{\varepsilon}_{eff} = d_T (\tilde{n}_{eff})^2 \,. \tag{46}$$

The counter-intuitive concept is first proposed by Smith *et al* [26], then detailed by Palpant *et al*[47]. They found that while the gold and ambient medium has positive thermo-refractive coefficient, the heterogeneous matrix has a large negative one at the LSPR, as demonstrated in Figure 1.

However, due to the operation of complex quantity $d_T \tilde{\varepsilon}_{eff}$ the effect of enhancement on the sign, width and LSPR position is not straight forward to $d_T \tilde{n}_{eff}$. Thus, in the following sections, we will discuss only the absolute value of these quantities.

doi:10.6342/NTU201602833

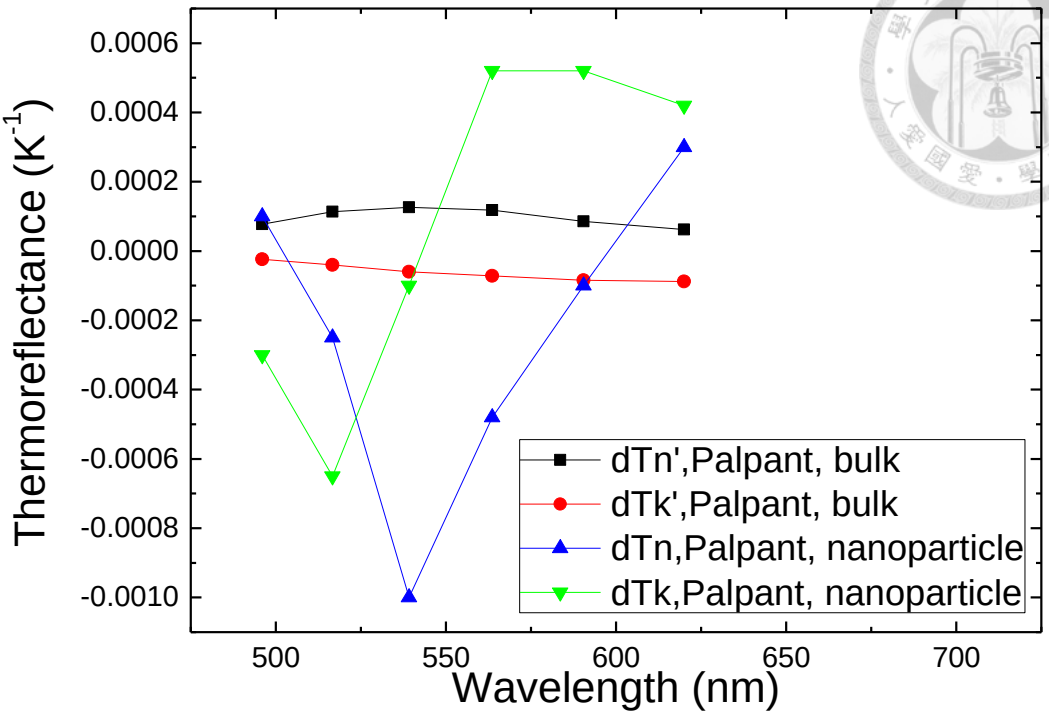

Figure 1. The comparison of thermoreflectance of gold nanoparticles (diameter 5nm) and bulk gold (As defined in (9), p=0.08). Replotted from [47].

2.5.2 Adaptation of Maxwell-Garnett theory on single-particle

Maxwell-Garnet formula is a formulation that works with matrix. Conventionally, the volume fraction is defined as the ratio of A_{sphere} (area of the sphere) to A_{total} (the total area), namely,

$$p = \frac{A_{sphere}}{A_{total}} \tag{47}$$

In the single-particle case, the total area cannot be determined. Therefore, the formula needs to be modified. The new volume fraction is written as

$$p = \frac{A_{sphere}}{A_{beamspot}} \tag{48}$$

Here the area of the sphere A_{sphere} is treated as a circular area. The area of the beam spot

doi:10.6342/NTU201602833

$A_{beamspot}$ should be seen as the area formed by full width at half maximum (FWHM) of the diffraction-limited Gaussian beam, which is $\pi D_{FWHM}{}^{2}/4\ln 2$. Therefore, *p* is now a function of sphere radius, incident wavelength, and numerical aperture (N.A.). In Figure 2, the resonance shifts as *p* increases. Nevertheless, the adaptation of Maxwell-Garnett theory to single-particle version fails. Table 1 is an attempt to find corresponding *p* for various particle size. With Eq. (45), we appointed *p* for each LSPR of respective particle size. However, applying Eq. (48) to each particle size clearly underestimates *p*. Hence, the Maxwell-Garnett theory only provides a hint to the thermal derivative around LSPR.

Radius(nm)	***Resonance(nm)***	***p calculated by*** (48)	***p fitted with*** (45)
<20	550	<0.03	<0.08
30	564	0.05	0.013
40	584	0.09	0.3

Table 1 Demonstration of newly defined p. Each p is linked to a specific particle diameter and a respective resonance.

It is also worth noting that larger *p* gives larger amplification, which might support Huang's conclusion on the particle-size dependence of the nonlinearity [28].

doi:10.6342/NTU201602833

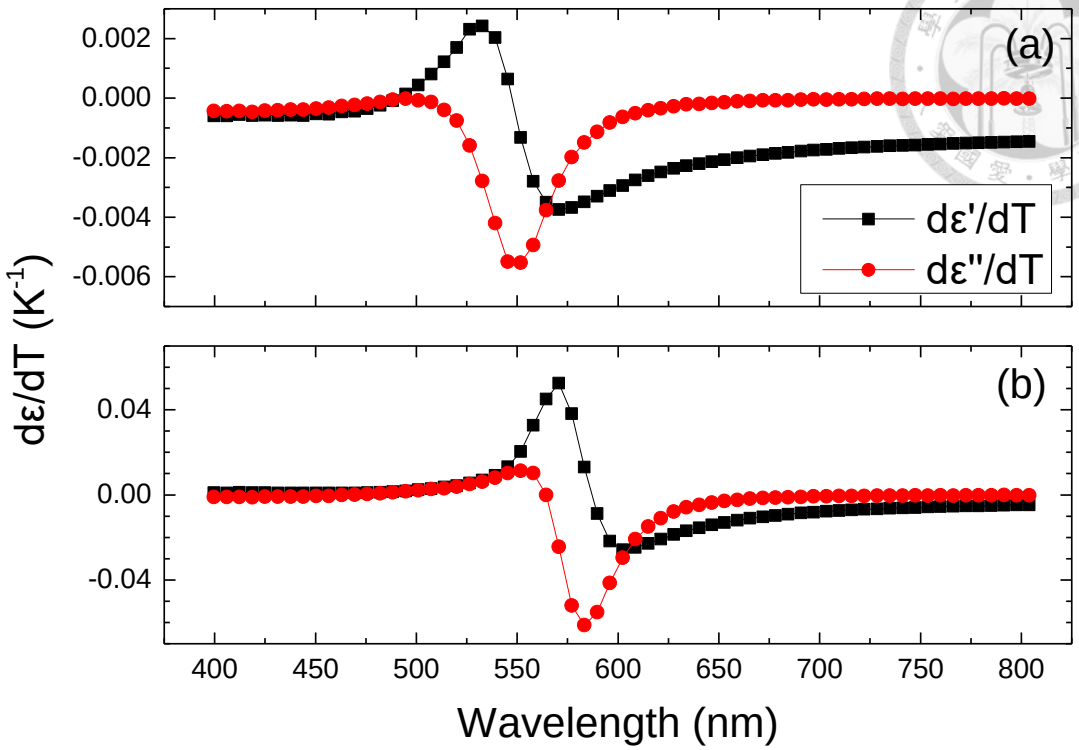

Figure 2. Calculation of Maxwell-Garnet formula with different volume fraction (a) p=0.08 and (b) p=0.3; Assume the temperature dependence of the ambient medium to be $d_T n_{med}$=-3×10^{-4} K^{-1}; Temperature-dependence extracted from our measurement.

2.5.3 The contribution of ambient medium

The Maxwell-Garnett formula considered both contribution from the inclusion and the ambient medium. To quantitatively examine the ambient medium contribution, we first calculate $d_T\tilde{\varepsilon}_{eff}$ with $d_T n_{med}$ set to zero, then assume a reasonable $d_T n_{med}$ based on reported value [32] to perform the same calculation.

Figure 3 shows that the ambient has a remarkable influence on the result. In Figure 3(b), the absolute maximum of themoreflectance is at 561nm. Surprisingly, even $d_T n_{med}$ is a real number, it has noticeable influence on $d_T\tilde{\varepsilon}_{eff}$. If we compare the absolute $d_T\tilde{\varepsilon}_{eff}$ on resonance to that of the off resonance (e.g 405nm), the amplification can be more than

doi:10.6342/NTU201602833

one order. That is, the enhancement at the LSPR increases. On the other hand, the ambient medium is responsible for majority of the change in real part, although the amplification is globally. To sum up, the ambient medium provides extra modulation depths based on the original modulation of metal.

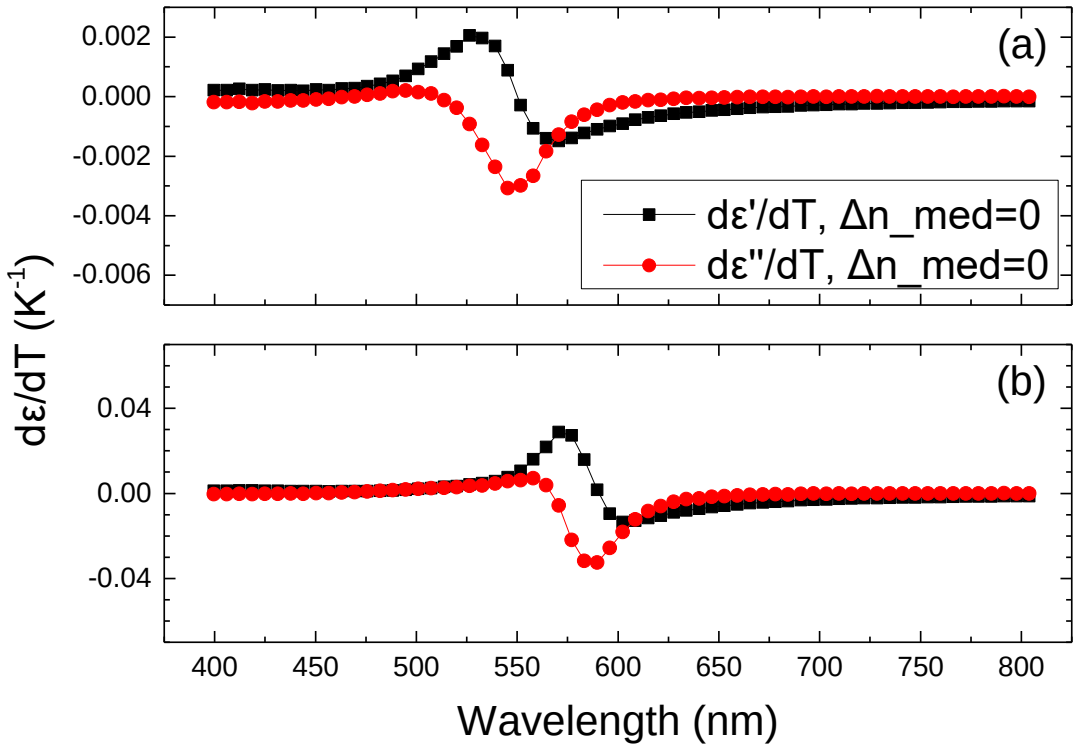

Figure 3. Calculation of Maxwell-Garnet formula with different volume fraction (a) p=0.08 and (b) p=0.3. Assume the temperature dependence of the ambient medium to be $d_T n_{med}$ =0

2.6 Hints from Maxwell-Garnett theory

As we mentioned in previous section, due to the operation of complex quantity $d_T\tilde{\varepsilon}_{eff}$, the effect of enhancement on the sign, width and LSPR position is not straight forward to $d_T\tilde{n}_{eff}$ .There is an implicit way to implement the enhancement to Mie scattering of the gold nanosphere. In previous section, it is clear that the $d_T\tilde{n}_{eff}$ is

doi:10.6342/NTU201602833

amplified around the LSPR, and the amplification rate is one order. We then convert $d_T \tilde{n}_{eff}$ to $d_T \tilde{\varepsilon}_{eff}$ by the relation

$$\varepsilon_1 = n^2 - \kappa^2 , \tag{49}$$

and

$$\varepsilon_2 = 2n\kappa , \tag{50}$$

where ε_1 is the real part of permittivity, and ε_2 is the imaginary part of permittivity. Surprisingly, $d_T \varepsilon_1$ has barely any amplification (amplification rate less than half an order), while $d_T \varepsilon_2$ still has at least one order larger amplification around the LSPR.

Thus, we have the effective permittivity for nanoparticle, which is

$$\tilde{\varepsilon}_{eff}(T) = \tilde{\varepsilon}_{eff}(T_0) + \Delta\tilde{\varepsilon}_{eff} , \tag{51}$$

where

$$\Delta\tilde{\varepsilon}_{eff} = \Delta\varepsilon_1 \times A_1 + \Delta\varepsilon_2 \times A_2 . \tag{52}$$

Here, A_i is enhancement determined by the ratio of absolute value of $d_T \varepsilon_i$ at on-resonance to $d_T \varepsilon_i$ at off-resonance. (51) is an amplification to (41) around the LSPR.

To obtain A_i empirically, we must normalize $Q_{sca}(T_0)$ and assume a reasonable amplification rate (m_i). Therefore,

$$A_i = m_i \times Q_{sca}(T_0) / \max(Q_{sca}(T_0)) , \tag{53}$$

where m_i is a number at the order of 10^1. m_i can be evaluated through the ratio of on-resonance $d_T \tilde{\varepsilon}_{eff}$ to that of the off-resonance.

doi:10.6342/NTU201602833

Chapter 3 Experiments

3.1 Sample preparation

3.1.1 Gold nanospheres

For single-particle scattering modulations, we use commercial gold nanospheres with 60-nm and 80-nm diameter (EM. GC 60, and EM. GC 80, BBI Solutions). The solution of nanospheres is dispersed onto adhesive microscope slide (Polysine Adhesion Slides $25\times75\times1$ mm, Thermo Scientific), then dehydrated. A droplet of immersion oil (n=1.518, type F, Olympus) submerges the dehydrated particles before the particles being sealed with cover glass ($18\times18\times0.17$ mm, Menzel-Gläser).

3.1.2 Bulk gold

For measurement of the bulk gold temperature-dependent permittivity, the gold film was made by electron beam evaporation of gold with 99.99% purity onto a silicon nitride substrate with 5nm titanium as an adhesion layer. Its thickness is 130±16 nm, which is enough to fully block transmission, and to be treated as a bulk sample [48]. For unannealed sample, the deposited film is directly used. For annealed sample, the gold film is placed at 600K for 15 minutes, under 10^{-3} atm, and then cooled off to 300K.

3.1.3 Immersion oil

For measurement of immersion oil temperature-dependent refractive index, we use (n=1.518, type F, Olympus). The constituents can be found in the expired patent [49], which are mainly liquid paraffins.

doi:10.6342/NTU201602833

3.2 Experiment setup

3.2.1 Confocal microscope equipped with spectral detection for single-particle experiments

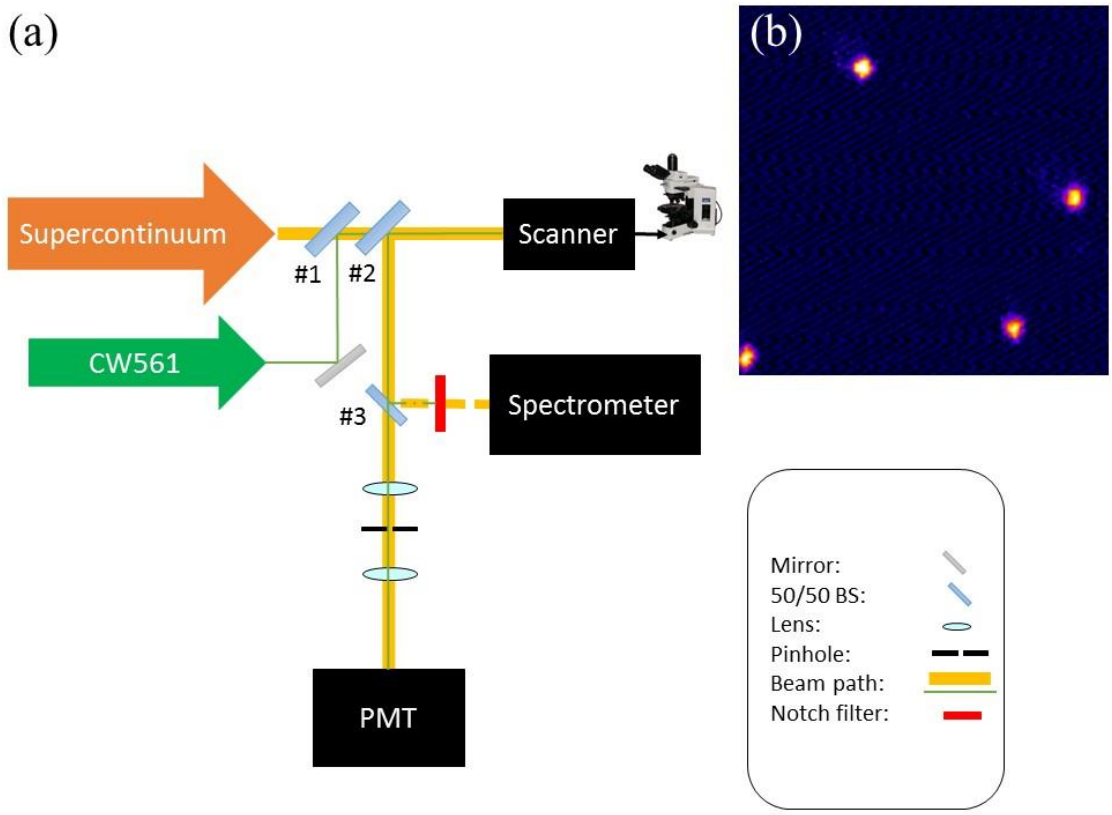

Figure 4. (a) Experimental setup, consisting of a confocal microscope, a hot plate on the microscope, a supercontinuum (WL-SC-400-2, Fianium Ltd.) with 200ps output pulsed width, a spectrometer (Shamrock 163 with iDus Cameras DV420A-OE, Andor Technology), and a PMT (H5783-01, Hamamatsu). The confocal microscope is composed of a custom galvo scanning system, upright microscope (BX-53, Olympus), and a 100x objective. (b) Image of single-particles under confocal microscope. Field of view: 25μm ×25μm

Our setup is a reflection confocal imaging system, combined with a supercontinuum

doi:10.6342/NTU201602833

and a spectrometer for spectral measurement, as shown in Figure 4(a). The light source of the confocal imaging part is a 561-nm CW laser. The laser is sent into a galvo scanning system to form two-dimensional raster scan at the focal plane of the objective. The backscattering signal of the particle is collected by the same objective and is separated from the incident beam with a 50/50 beamsplitter (#2 in Figure 4(a)). Then the signal is focused at the confocal pinhole to eliminate out-of-focus contribution, and detected by a photomultiplier tube (PMT). Figure 4(b) shows an image of particles under the confocal system.

Another laser source in the system is a supercontinuum source, which serves as a "probe" for spectroscopic detection. It is combined with the 561-nm laser (#1 in Figure 4 (a)), and shares the same beam path until being split in front of the spectrometer by another 50/50 beamsplitter (#3 in Figure 4(a)). Half of the backscattered supercontinuum signal is received by the spectrometer, in front of which a notch filter (NF561-18, Thorlabs) is placed to block excess 561-nm laser. Another half goes to the PMT to form the confocal images.

With the setup, we conduct three different experiments: the intensity dependence of nonlinear scattering, thermally induced spectrum variation with hot plate, and optically induced spectrum variation with CW laser. Each of the experiment uses slightly different components.

The intensity dependence test involves only the images formed by the backscattering of 561-nm CW laser. To get the intensity dependence of nonlinear scattering, images at different intensities are taken, and the corresponding point spread functions are extracted. The values at central pixels of each point spread function are averaged to be the scattering intensity.

In the thermally induced spectrum variation measurement, the images and spectra

doi:10.6342/NTU201602833

formed by the supercontinuum are analyzed.

In Figure 5, we demonstrate how to acquire a single-particle scattering spectrum [50]. To collect a single-particle backscattering spectrum, the laser focus should be placed on top of the particle, and the backscattering from that particle is guided into a spectrometer (Figure 5 (a)). Next, we place the focus on the surroundings of the particle to collect the background reflection (Figure 5 (b)). The reference spectrum (Figure 5 (c)) is taken with a silver mirror at focus. Finally, the single-particle scattering (Figure 5 (d)) is obtained by [(a)-(b)]/(c).

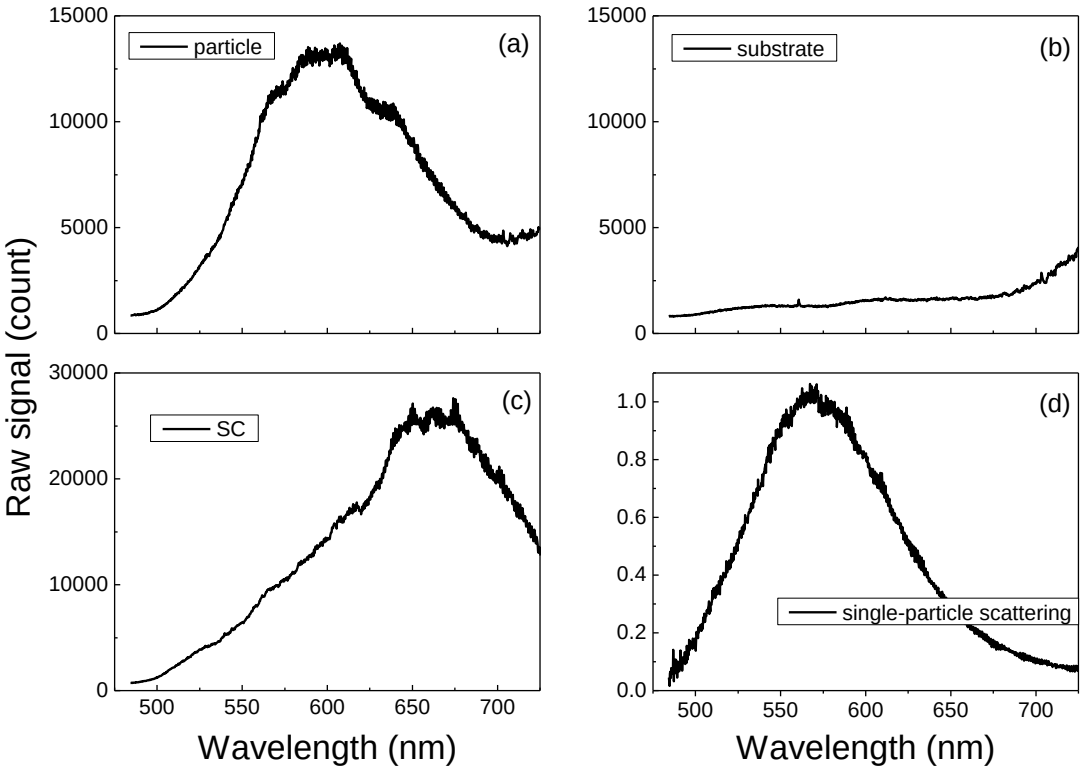

Figure 5. The (a) single-particle backscattering (b) reflection from the substrate of an isolated particle. (c) The reference of the supercontinuum source. (d) The single particle scattering determined by [(a)-(b)]/(c). Replotted from [50].

At each temperature, an image of a group of single particles is taken along with the spectrum. In Figure 6, when the temperature rises, the particle drifts due to thermal

doi:10.6342/NTU201602833

expansion of the substrate and stage, and we have tracked the same particle (Figure 6 (a) and (b)) with the aid of image to take temperature-dependent spectrum. In Figure 7, as the temperature rises, the signal from single-particle backscattering decreases significantly, while the signal from the substrate slightly increases. Thus, the amplitude modulation of single-particle scattering is shown to be mainly contributed by the nonlinearity of the gold nanoshere.

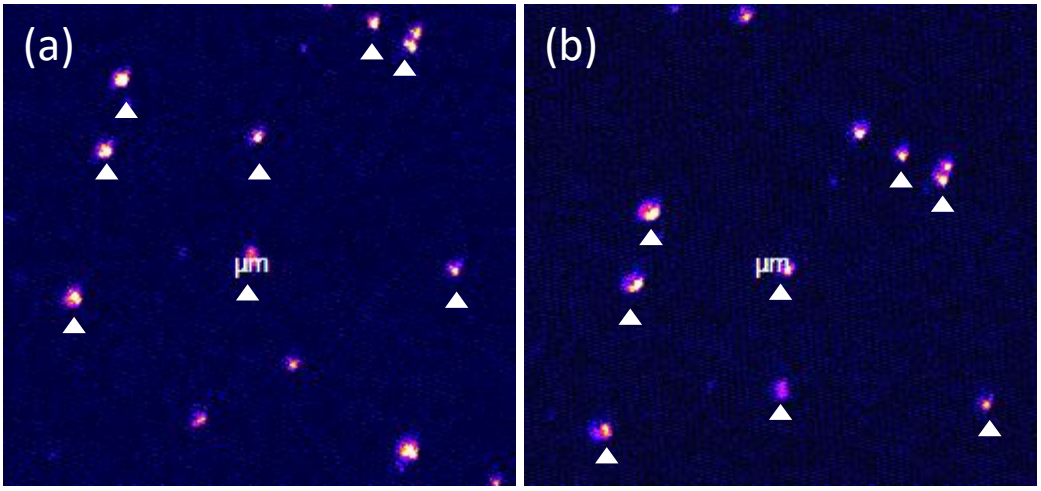

Figure 6. The confocal image of (a) 300K (b) 325K. The center is marked by the text "μm". The white triangles marks the nanoparticles being tracked. Field of view: 50μm× 50μm

doi:10.6342/NTU201602833

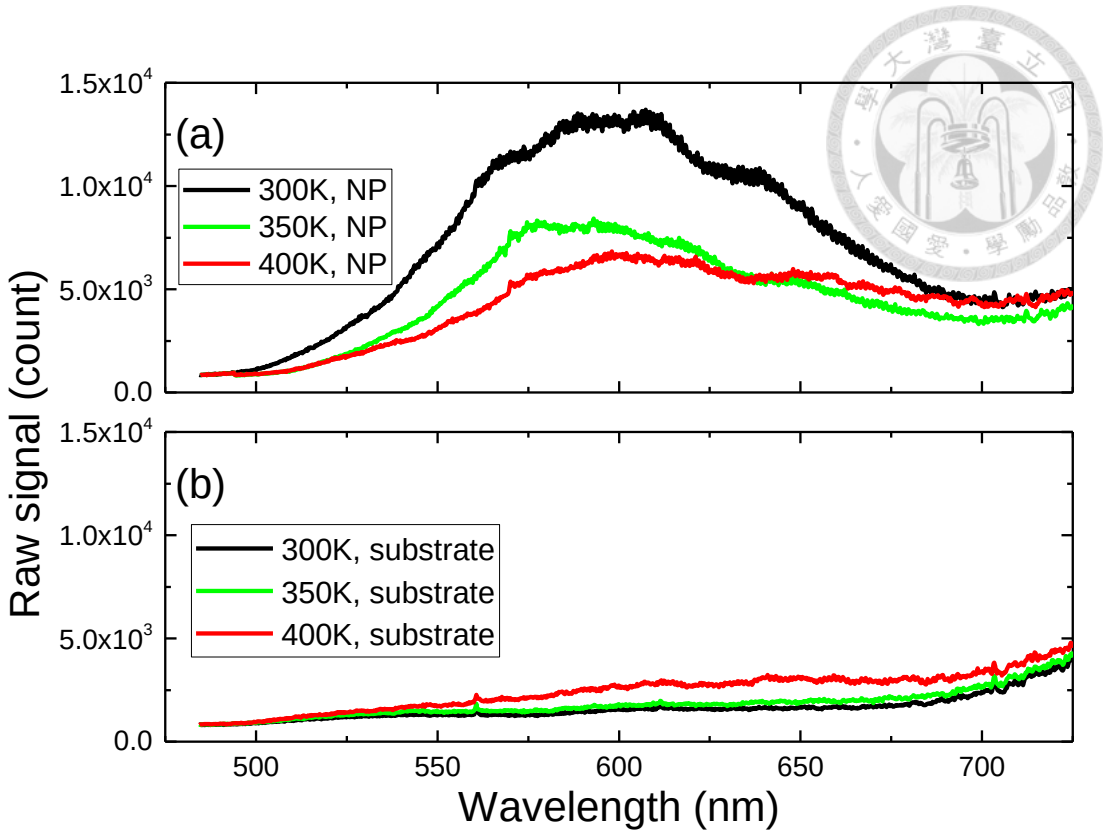

Figure 7. The (a) single-particle backscattering (b) reflection from the substrate of an isolated gold nanosphere (80nm as diameter) at different temperatures.

In the optically induced spectrum variation measurement, both lasers are involved. First, we aligned both lasers, making them overlapped at the pinhole. An image is taken, along with corresponding spectrum with the CW laser blocked. Then we turn on the CW laser to optically heat up the particle and record backscattering spectrum from supercontinuum as the power of CW laser increases. The results can be compared with the hot plate heating experiment to check the validity of hot lattice mechanism.

doi:10.6342/NTU201602833

3.2.2 Temperature-dependent ellipsometry

The temperature dependent permittivity was acquired with a spectroscopic ellipsometry (M2000 U, J.A. Woollam Co, NE) from 190 to 1600 nm. The thermal loading was done by hot plate in a vacuum chamber (10^{-3} atm). The measurement range was supposed to be 300 to 700K. However, the sample could be damaged beyond 570K. Consistent measurement results were all taken from 300 to 570K. The calibration was done by taking sequential measurements at 570K until there's only random error in the readings.

3.2.3 Abbe refractometer

The temperature dependence of the refractive index was measured by Abbe refractometer (ATAGO NAR-3T) from the Department of Chemical Engineering National Taiwan University (With refractometer, only the refractive index in lower temperature range can be measured), and compared to the reported value [32]. The temperature control was done by water bath. The measurement range was from 296 to 323K.

3.3 Experiment results

3.3.1 Intensity dependence of single-particle nonlinear scattering

In Figure 8, we gradually increases the excitation intensity of 561nm-CW laser. Below 1 MW/cm^2, the scattering intensity is linear. Then, the scattering becomes nonlinear and lower than the linear trend (saturable) around 1 MW/cm^2. If the excitation intensity further increases, the scattering exceeds the linear trend (reverse saturable). Combining the equations in 2.2 to fit the saturable curve in Figure 8, we found the value of n_2 to be 3.0×10^{-7} cm^2/W, which is closest to the hot lattice range (>10^{-8} cm^2/W), as given in 2.2. Therefore, we propose that the most possible mechanism is hot lattice. From

doi:10.6342/NTU201602833

this proposition, the nonlinear scattering can be caused by either shift or weakening of the LSPR. Therefore, heating plus spectroscopic measurement is necessary to further clarify the mechanism.

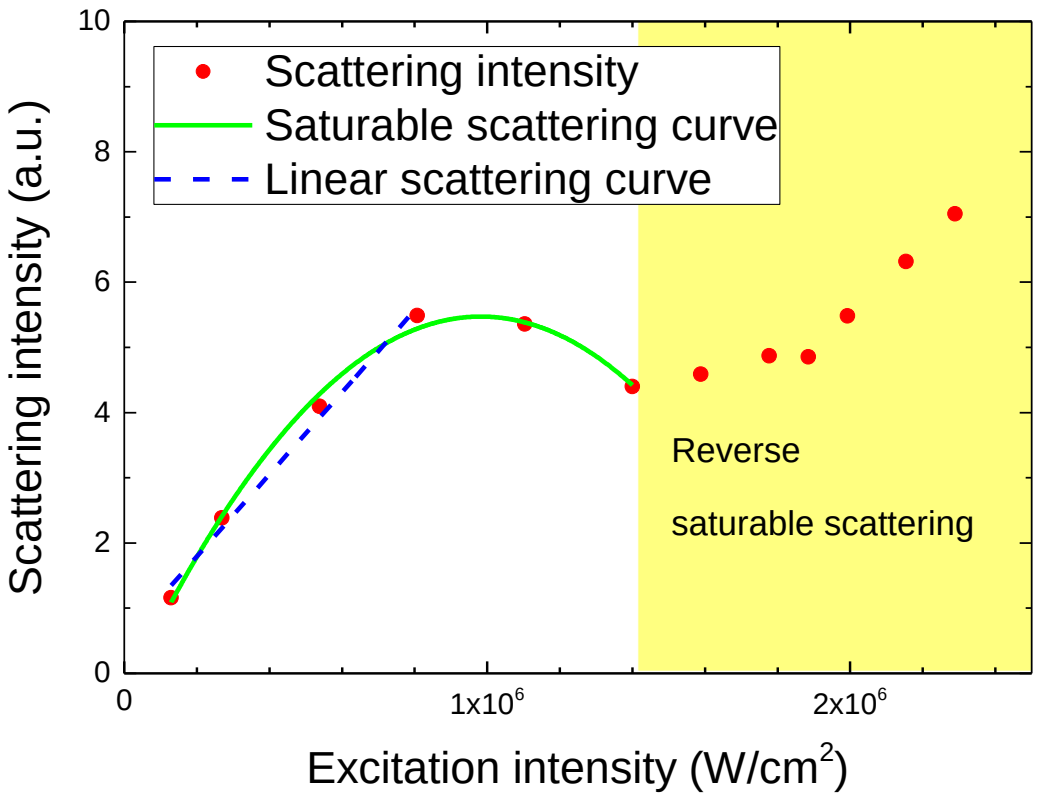

Figure 8. Intensity dependence of nonlinear scattering by 561-nm CW laser. Red dots are the scattering intensity of the laser. At low intensity, the red dots form a linear relationship, as shown by the blue dashed line. On the other hand, the nonlinear scattering curve (green line) and the corresponding n_2 is determined by fitting the red dots with equation (16).

3.3.2 Single-particle scattering modulation by CW

In this section, we check the LSPR spectrum by optical heating with the 561-nm CW laser. Figure 9 shows the scattering spectrum of a gold nanosphere at different laser intensities. Under the excitation intensity of 0.4 and 0.7 MW/cm^2, the scattering intensity

doi:10.6342/NTU201602833

decreases compared to zero excitation. Also, the LSPR is weakened, but not shifted. We notice the sidelobe around 700nm. According to Mie theory (Figure 15), the scattering intensity of the off-resonance should be 10% the scattering intensity of the on-resonance. This sidelobe is probably due to the offset during acquisition of the reference spectrum or reflection of the substrate.

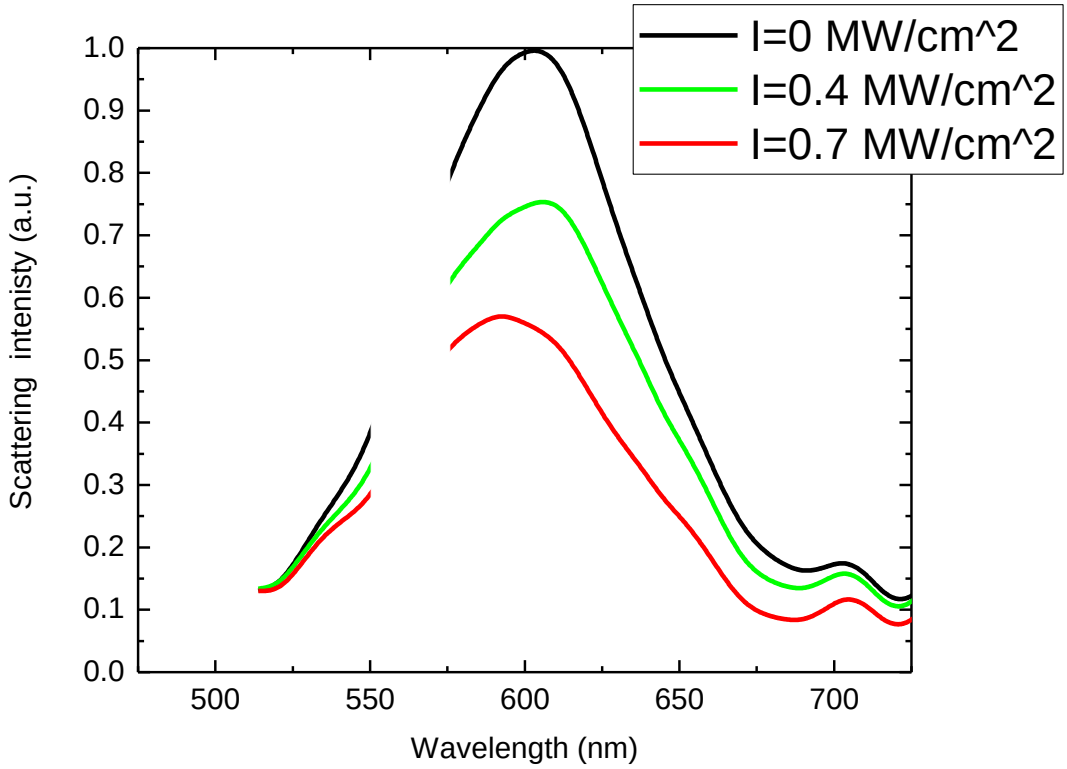

Figure 9. As the excitation intensity of 561nm CW laser increases, the scattering intensity of supercontinuum decreases. The blank of the spectrum is due to the notch filter that protects the spectrometer from excess 561nm laser.

3.3.3 Single-particle scattering modulation by environmental heating

In previous section, we have shown that optical heating causes scattering spectrum reduction, but not shift. In this section, we heat up the sample with a hot plate and measure scattering spectrum from a single particle. As the temperature increases, the scattering

doi:10.6342/NTU201602833

intensity decreases across the whole LSPR spectrum, as shown in Figure 10. Quantitatively, for nanospheres with 80nm-diameter (Figure 10 (a)), the scattering becomes 40% weaker by heating up only 50 kelvins above room temperature, and becomes 70% weaker by heating up 100 kelvins. Apparently, change of temperature does weaken the LSPR, but not significantly shift it. Combined with Mie theory [25], this result implies that the permittivity changes mainly in imaginary part as the temperature increases. If we also track the same 60nm-diameter particle (Figure 10 (b)), similar behavior is observed.

Another important implication from the comparison between hot plate and optical excitation experiment is to exclude the electron transition that might be caused by the 561-nm CW laser, whose photon energy is 2.21 eV. By heating up the particle with 100 K, the equivalent thermal energy transfers to electrons is less than 0.01 eV ($\hbar\omega = k_B T$), which is much smaller than photon energy.

In addition, in Figure 9 and Figure 10, the peaks of LSPR are slightly different to each other. The possible reason for this deviation in resonance may be size variation of the particles, even though the gold nanospheres in the two experiments are from the same commercial gold nanospheres. In the future, not only statistic study of nonlinear scattering with different nanoparticle diameters will be carried out, but the quantitative model to link optical intensity and nanoparticle temperature will also be established, as well as the temperature dependent permittivity, to fully account for the mechanism of nonlinear scattering.

doi:10.6342/NTU201602833

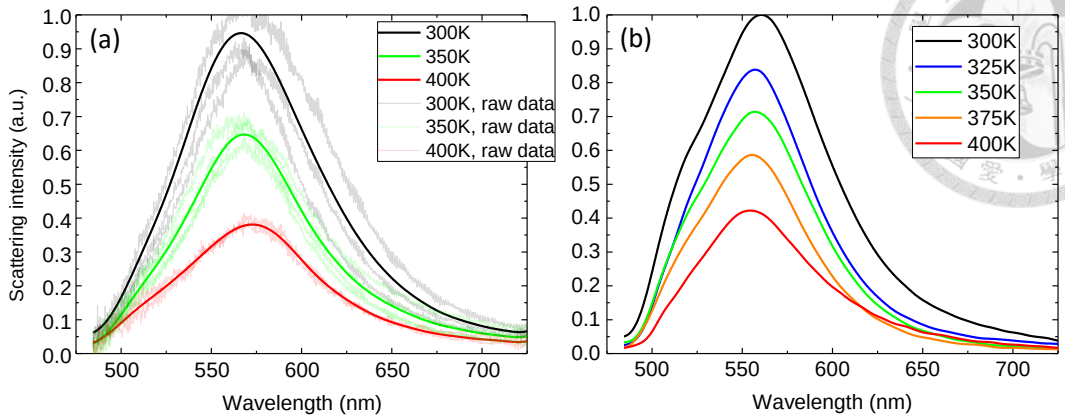

Figure 10. Heating the gold nanospheres by a hot plate to induce significant scattering variation. (a) Statistics on the scattering intensity of 80nm-diameter gold nanosphere at different temperatures. Thick-solid line: averaged scattering intensity; Thin-light line: raw data. (b) Tracking the same 60nm-diameter gold nanosphere with finer temperature resolution.

3.3.4 Temperature-dependent bulk gold permittivity

From 3.3.2 and 3.3.3, the permittivity changes mainly in imaginary part as the temperature increases. In order to calculate the modulation caused by variation in permittivity with Mie theory, we measure the temperature dependence of bulk gold permittivity. Interestingly, the result is very different in two thermal cycles given to the sample. We examine the variation carefully. First, the first thermal cycle (noted as before annealing or unannealed) gives much less optical loss (lower imaginary part) compared to well recognized data of Johnson and Christy [51]. However, in the second thermal cycle (noted as after annealing or annealed), the optical loss becomes larger and matched to Johnson and Christy's result. We have thoroughly argued that this anomaly is probably due to the *in-situ* annealing effect on the morphology in our paper [33]. The point is that previous measurements of temperature-dependence permittivity [52, 53] have to be looked at very carefully when being adopted in thermo-plasmonic calculations.

doi:10.6342/NTU201602833

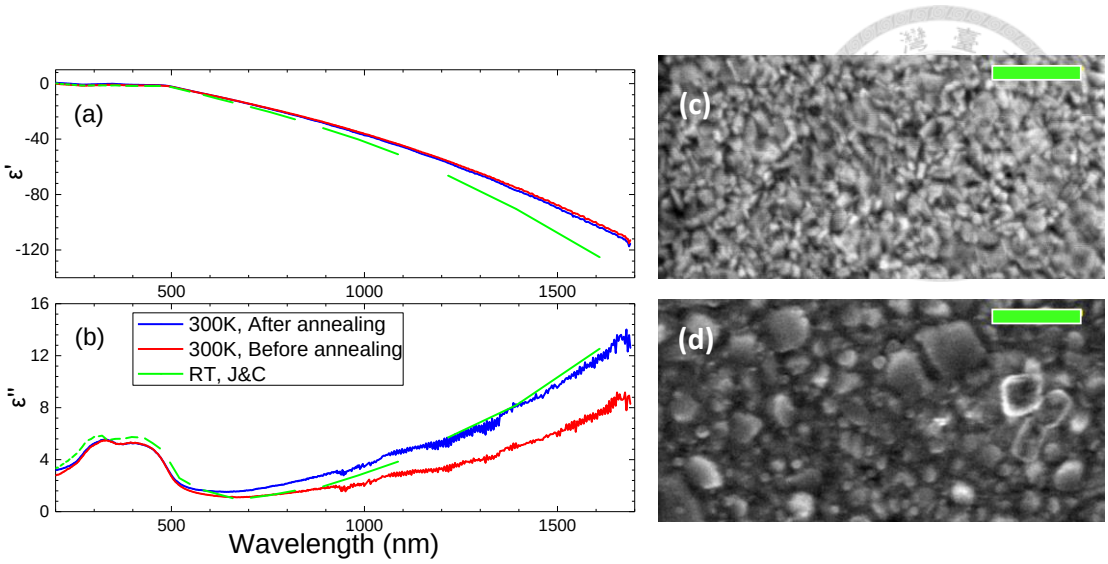

Figure 11. (a) The real part ε' and (b) imaginary part ε" of permittivity of gold at room temperature. Morphology (c) before annealing (d) after annealing. Scale bar: 400nm. Replotted from [33].

With the knowledge that morphology dictating the temperature dependence, we next discuss the data of our measurement. By increasing temperature gradually on an unannealed film, remarkable variation of gold permittivity throughout the spectral domain is observed. The results of several representative wavelengths in the visible range are given in Figure 12. For the real part in Figure 12(a), the data below 500nm exhibits only slight variation. The variation is more and more significant for increasing wavelength, with the same trend of decrease and then increase above 460K. On the other hand, for the imaginary part in Figure 12(b), monotonically increase is observed for wavelengths above 500 nm; while for 400 and 500 nm, the trend is increase and then decrease above 460K.

To highlight the variation, the thermo-derivatives of real and imaginary parts of the permittivity are given in Figure 12(c) and (d), respectively. In Figure 12(c), very interestingly, all wavelengths exhibit the same trend of being negative or smaller at low

doi:10.6342/NTU201602833

temperature, and becoming positive or larger above 460K, with a peak showing largest variation at around 500K. For the imaginary part in Figure 12(d), similar trends are also seen for all wavelengths, decreasing from positive at low temperature, and reverting to increase at 450 – 500K. Here, only wavelengths below 500nm exhibit negative derivation at high temperature.

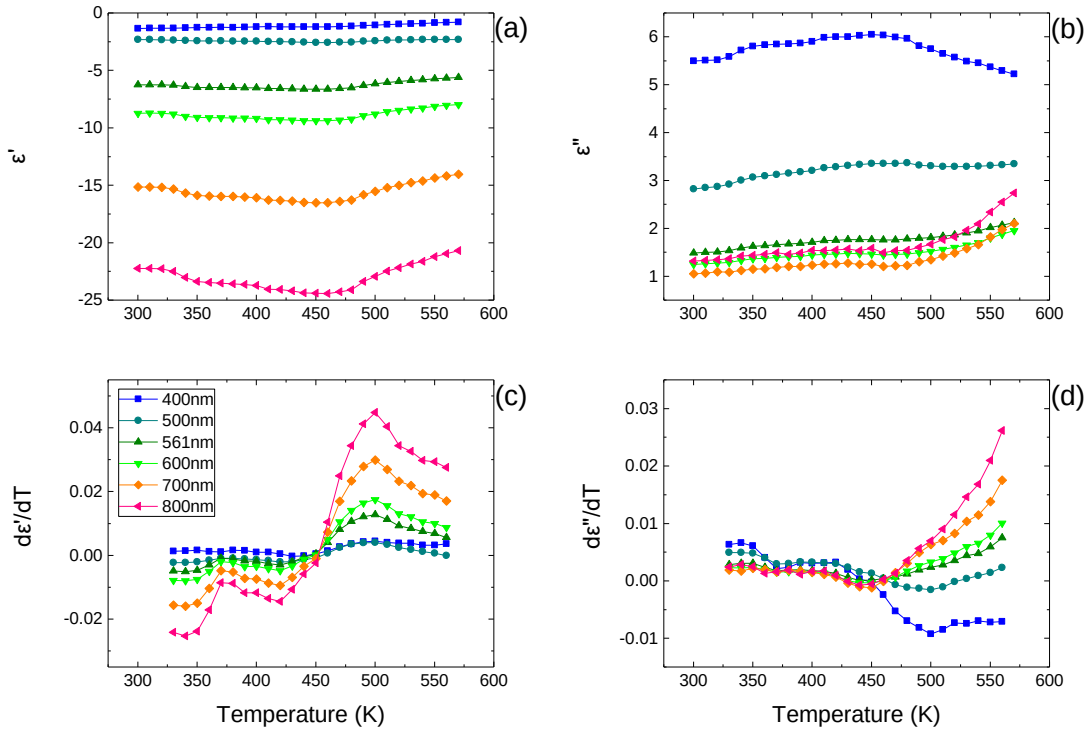

Figure 12. The real part ε' and (b) imaginary part ε" of permittivity with unannealed gold films in the visible band. (c) and (d) are the thermo-derivatives of ε' and ε".

doi:10.6342/NTU201602833

Figure 13(a) and (b) show the permittivity of the annealed gold film with increasing temperature. Compared to the unannealed film in Figure 12, the variation is much less, and also much smoother. For both the real and imaginary parts, almost perfect linear trends are observed, with less than 4% error, agreeing well with [54]. In Figure 13(a), for 400 and 500 nm, the overall permittivity variations are ~10 and -20%; while for wavelengths above 500nm, the permittivity variations are less than 5% (even 1% at 800nm), from 300 to 570K. On the other hand, in Figure 13(b), for 400nm and 500nm, the permittivity variations are less than 6%; while for wavelengths above 500nm, the variations are all larger than 20%.

The corresponding thermo-derivatives of real and imaginary parts are drawn in Figure 13(c) and (d), respectively. Except 400 and 500 nm, other wavelengths exhibit similar trends. In the real part, the thermo-derivatives reduce at low temperature, and start to increase at 500K. In the imaginary part, the thermo-derivatives increase monotonically. Comparing to Figure 12(c) and (d), the thermo-derivatives of the annealed film is one order smaller than the unannealed film.

doi:10.6342/NTU201602833

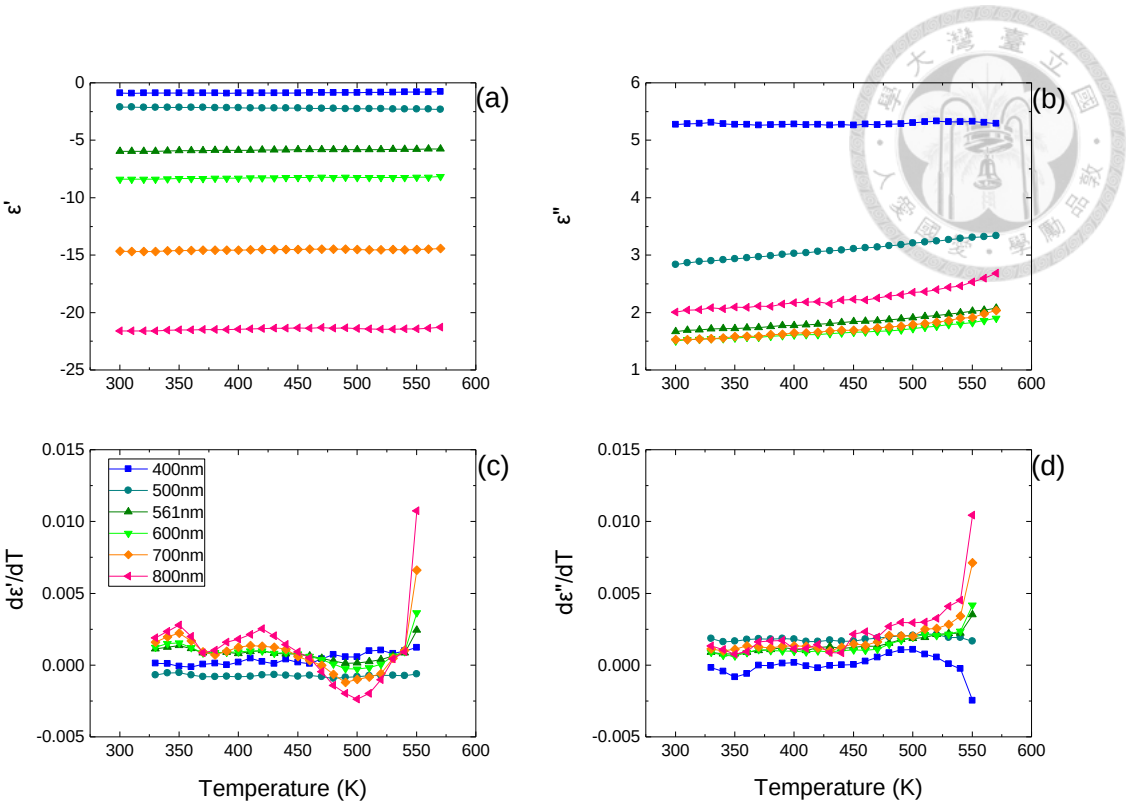

Figure 13. (a) The real part ε' and (b) imaginary part ε'' of permittivity with annealed gold films in the visible band. (c) and (d) are the corresponding thermo-derivatives of ε' and ε''.

In typical Drude model, the effective electron mass decreases as the temperature rises, so the $\frac{d\omega_p}{dT}$ should be positive ($\frac{d\varepsilon_1}{dT}$ is thus negative). Therefore, the unannealed film (negative $\frac{d\varepsilon_1}{dT}$) is closer to theoretical prediction (blueshift) below the annealing temperature, and we will use its permittivity for most of the calculations in the thesis.

3.3.5 Temperature-dependent immersion oil refractive index

The temperature dependence of oil is measured in the temperature range of 296 to 323K. The intercept is 1.515, and the slope $d_T n_{med}$ is -3.65×10^{-4}. The reported values for immersion oil $d_T n_{med}$ are -3.00×10^{-4} [55]. Although the proportion of constituents

doi:10.6342/NTU201602833

might be different (different brand and model number), the measurement still matches the reference. It also implies that the oil should have minor effect on the modulation depth since the oil refractive index does not change significantly.

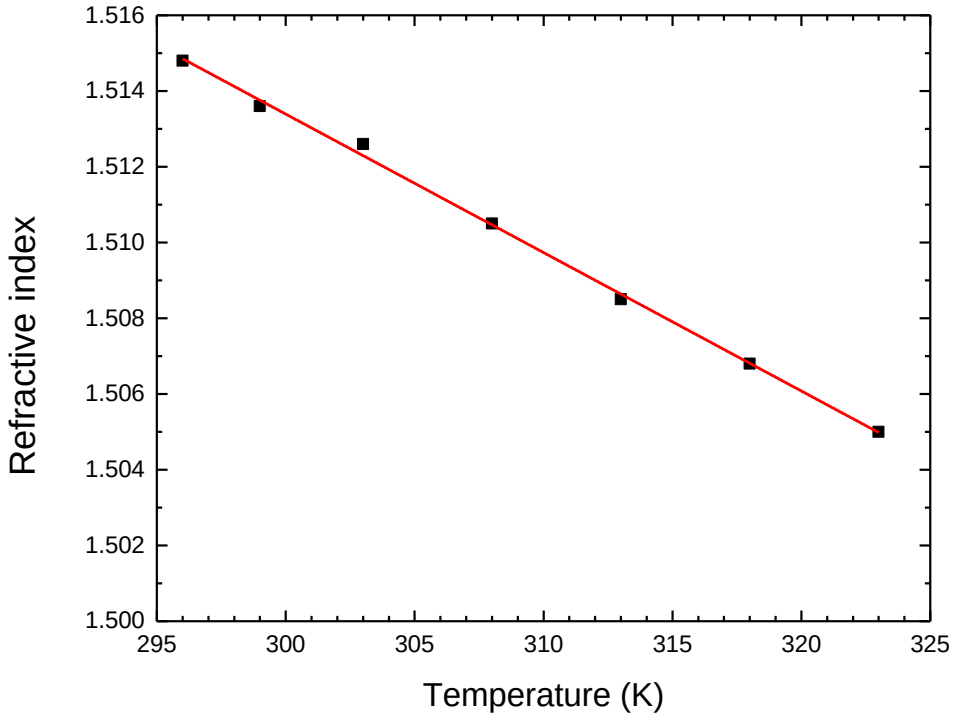

Figure 14. Temperature dependence of oil index.

3.4 Discussion

In 3.3.1, we experimentally derive the nonlinear refractive index (n_2) for nonlinear scattering in gold nanospheres, and make a comparison to four candidate mechanisms: intraband transition, interband transition, hot electron, and hot lattice.

doi:10.6342/NTU201602833

Mechanism	**Temporal scale**	$\mathbf{n_2}(cm^2/W)$
Intraband	10^1 fs	10^{-12}
Interband	10^1 fs	$10^{-12} \sim 10^{-10}$
Hot electron	10^3 fs = 1ps	$10^{-10} \sim 10^{-8}$
Hot lattice	10^2 ps	$>10^{-8}$

Table 2 Nonlinear refractive indices and temporal scale. Listed in 2.2.

We find the n_2 of nonlinear scattering is closest to that of hot lattice, which should be the solid evidence for Huang's proposition [28]. The proposition is verified through the measurement of scattering spectrum variation induced by heating through a hot plate and heating through a 561-nm CW laser.

In 3.3.2 and 3.3.3, it turns out that scattering spectrum variation induced by heating and by laser exhibits similar pattern. From the hot plate experiment, we also exclude the possibility of optical transition by the 561-nm photon. In addition, in Figure 7, we show that the majority of the nonlinearity comes the isolated nanoparticle, and the immersion oil only has minor effect (in agreement with 3.3.5). Nevertheless, the measurement of bulk gold permittivity in 3.3.4 surprises us. Even in bulk gold measurement, the surface morphology still influence the optical properties severely. It again shows the difficulty in realization of LSPR devices.

doi:10.6342/NTU201602833

Chapter 4 Permittivity of single particle

4.1 Conventional Mie theory

In 3.3.4, the total variation in imaginary part from 300 to 400K in the visible band is ~10% for the unannealed film, ~5% for the annealed film. Figure 15 shows that Mie theory carries small $\Delta\tilde{\varepsilon}$ to small ΔQ_{sca}. With the variation in ambient medium considered, the total variation in Q_{sca} from 300 to 400K is ~20% for the unannealed film, ~10% for the annealed film. This variation is negligible when being compared to Figure 10. Thus, the quantity of nonlinearity cannot be calculated through conventional Mie theory.

We notice the resonance shift due to the variation in real part. In general, reducing the real part causes the resonance to blueshift, while increasing the real part causes the resonance to redshift. Below the annealing temperature (460K), in Figure 15(a), the resonance blueshifts. From 450 to the 570K, Figure 15(a) the resonance redshifts instead, but in Figure 15(b), regardless of the annealing temperature, there's only blueshift. However, in 3.3.4, the real permittivity of the annealed film only slightly increases. Hence, the blueshifts of Figure 15 mainly come from the ambient medium.

doi:10.6342/NTU201602833

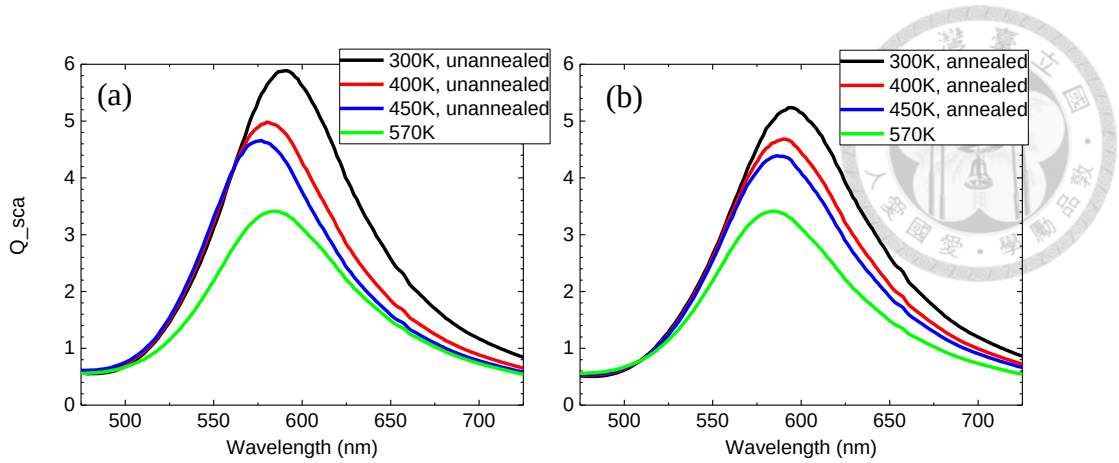

Figure 15. Calculated Mie scattering efficiency of 80nm gold nanosphere. Permittivity from (a) unannealed (b) annealed gold film. The temperature-dependent refractive index of ambient medium is extracted from 3.3.5.

4.2 Single-particle permittivity based on the hints from Maxwell-Garnett theory

In 4.1, the quantity of the nonlinearity is far from enough (compared to Figure 10). Now, we insert $\varepsilon_{eff}(T)$ in Eq. (51) to Mie theory. At the same time, $\Delta\varepsilon_{med}$ should be considered in the calculation to provide extra enhancement and compensate the slight resonance shift due to the variation in real permittivity. From Eq. (52), for p=0.3 (corresponding to the resonance of 80nm nanosphere), A_1 is at the order of $10^{1/2}$ and A_2 is at the order of 10^1. We thus select fitting parameters and plot the result in Figure 16.

Figure 16 is in excellent agreement with the experiment result in Figure 10. That is, Figure 16, for nanospheres with 80nm-diameter, the scattering becomes 38% weaker by at 350K, and becomes 72% weaker at 400K (both with the background subtracted).

Figure 17 shows that the real part of the $d_T n_{med}$ enhances the modulation depths by about 20% (-60% at 400K without $d_T n_{med}$), only qualitatively predicted by adapted Maxwell-Garnett theory. The temperature dependence of the ambient medium should not

doi:10.6342/NTU201602833

have significant effect, but still be considered.

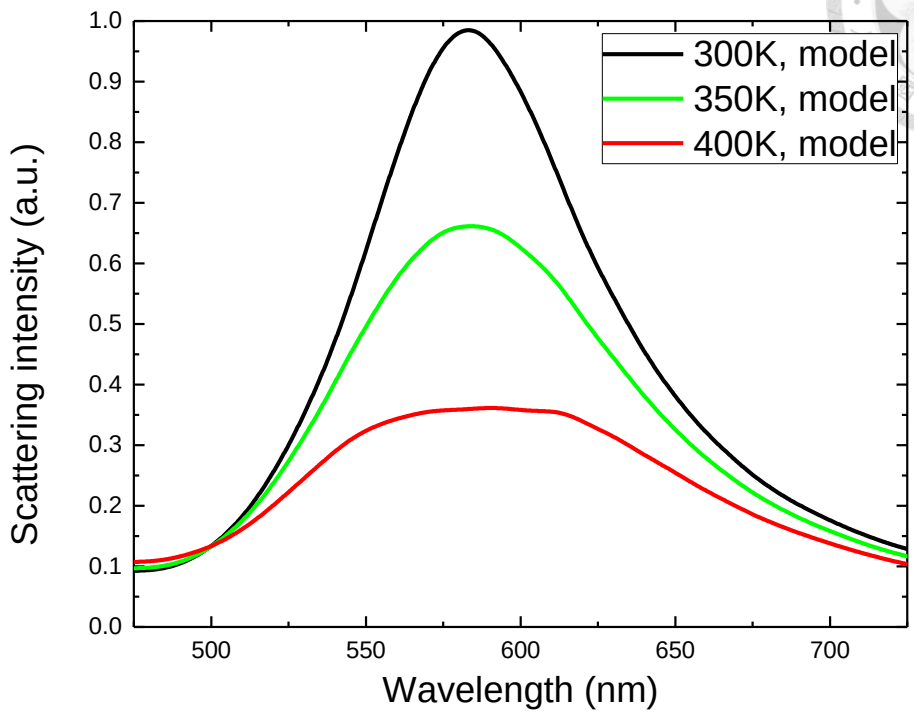

Figure 16. The calculated scattering modulation of 80nm gold nanosphere based on the hints from Maxwell-Garnett theory. Empirical parameters are A_1=1, A_2=7, Δn_{med} =-0.02 for 350K; A_1=3, A_2=14, Δn_{med} =-0.0365 for 400K

doi:10.6342/NTU201602833

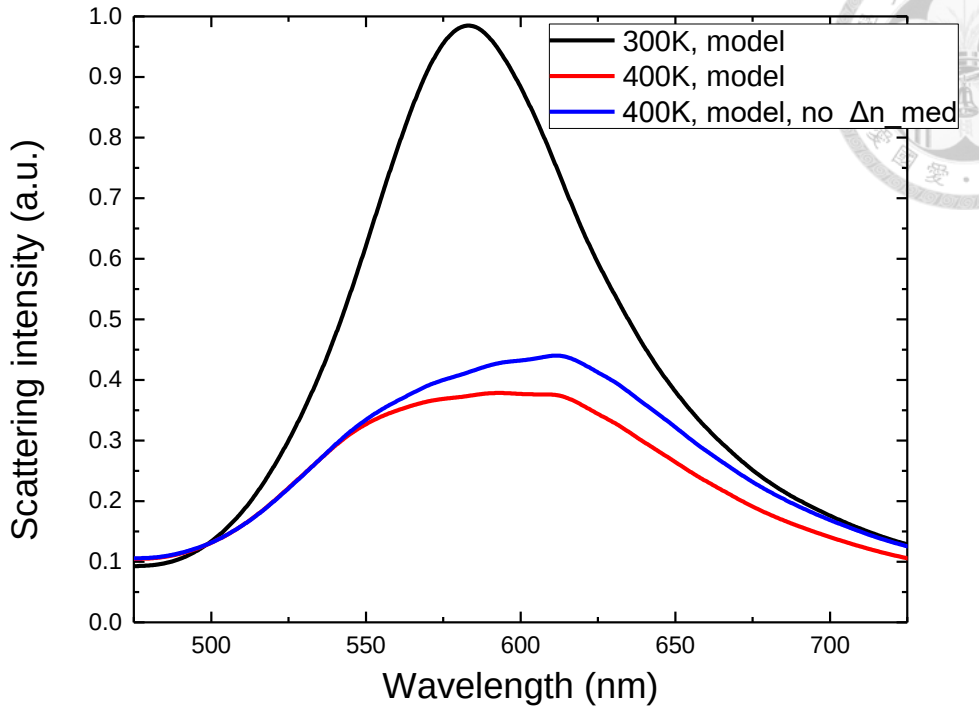

Figure 17. The calculated scattering modulation of 80nm gold nanosphere based on the hints from Maxwell-Garnett theory. Empirical parameters for the red curve are A_1=3, A_2=14, Δn_{med} =-0.0365 for 400K; for the blue curve A_1=3, A_2=14, Δn_{med} =0

What's more interesting is the hint hidden in this model. The nanoparticle has an obviously different permittivity than that of the bulk, as we show in Figure 16. Unfortunately, the hints do not give physical realization on A_i, and in general the Maxwell-Garnett theory doesn't work with single-particle systems. The volume fraction is clearly an oversimplified parameter on the local damping effect of electrons. Therefore, we try Lorentz-Drude model to describe such anomalous dielectric function on single particle. In Figure 18, there is an oscillator bandwidth which is roughly about 0.5~1 eV, stretching from 500 to 700 nm. It implies the existence of a fictitious oscillator.This parameter is keyto uncover the actual physical process of nonlinear scattering.

doi:10.6342/NTU201602833

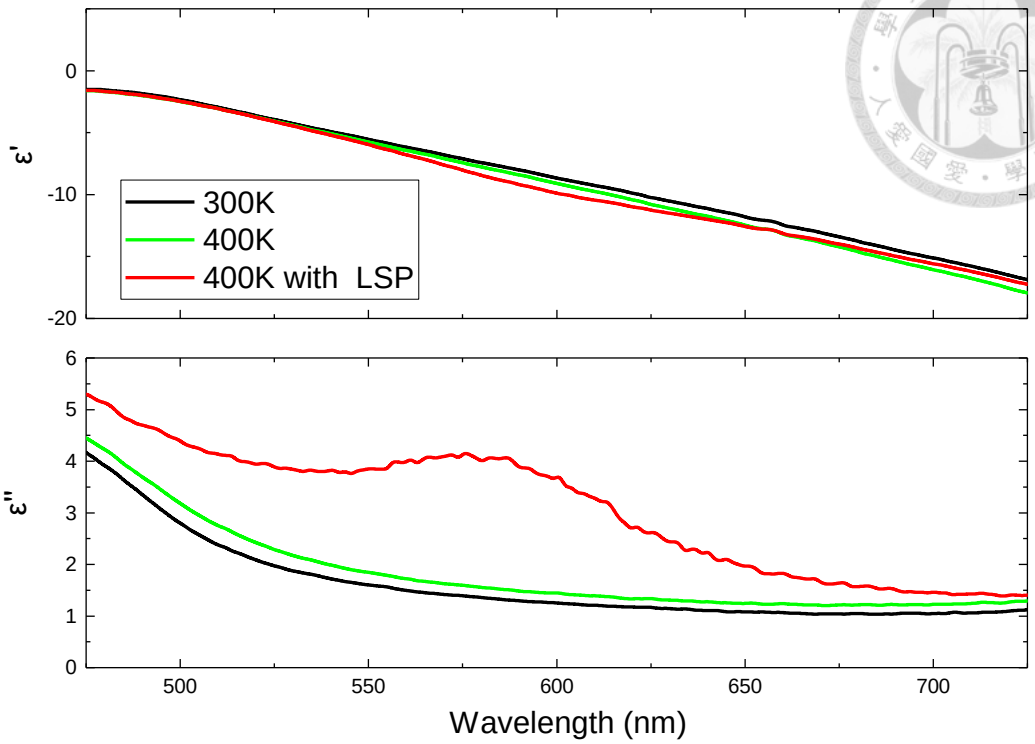

Figure 18. The effective permittivity derived from the hints of Maxwell-Garnett theory.

4.3 Model of single-particle permittivity: with damping of LSP

Lorentz-Drude model allows us to reconstruct such permittivity by simply adding a new oscillator at the LSPR. We introduce a fictitious oscillator ω_{LSP} to the Lorentz-Drude model that damps at the damping rate Γ_{LSP} with oscillator strength f_{LSP}.

First, we select reasonable damping rate Γ_{LSP} and oscillator strength f_{LSP} corresponding to ω_{LSP}. We adopt the five-pole Lorentz-Drude parameters of gold from [56]. In Table 2, there are two interband transitions close to the end points of visible band (1.55-3.1eV, i.e. 800-400nm). One is ω_3 close to the 400nm and another is ω_2 close to 800nm. The bandwidths are 0.345 and 0.87 eV respectively. The oscillator strengths are 0.01 and 0.071 respectively. In order to be physical, the fitting parameters should be

doi:10.6342/NTU201602833

of similar order.

m	0	1	2	3	4	5	LSP
	intraband	interband	interband	interband	interband	interband	
ω_m (eV)	0	0.415	0.83	2.969	4.304	13.32	1.55~3.1
Γ_m (eV)	0.053	0.241	0.345	0.87	2.494	2.214	~1
f_m	0.76	0.024	0.01	0.071	0.601	4.384	~0.01

Table 3 The room temperature fitting parameters of Lorentz-Drude model [56], and possible LSP parameters

Next, we assume the diameter of the nanosphere to be 80nm, which corresponds to resonance ω_{LSP} at 590nm (2.1 eV). When temperature of the plasmonic structure rises, the SP may be significantly damped due to the increase of electron-phonon scattering [5, 11]. The damping of SP is a process of decoherence in the collective electron oscillation (plasmons), i.e. dephasing. Such process is usually described by a simple two-level system, where the dephasing time for surface plasmons in colloidal gold is evaluated to be less than 5 fs [29]. Conventionally, the electron-electron interactions are regarded as dominant mechanism to the damping of SP. However, more recent study about heating plasmonic nanoparticles further found out electron-phonon scattering should be the real cause of SP damping, and interband transition also contribute significantly [10, 11].

In literature [11], the dephasing time by electron-phonon scattering above the Debye temperature (343K for copper) in copper nanoparticles (diameter ~10nm) is evaluated to

doi:10.6342/NTU201602833

be 10 fs or smaller. Such dephasing time even decreases to about 1 fs at the temperature twice the Debye temperature. Therefore, it is reasonable to assume the decaying time of electron-phonon scattering to be a few femtoseconds in our case, where the Debye temperature of gold is only 170K. We will discuss more details about the evaluation of electron-phonon scattering in 4.4.1.

More interestingly, the decaying time of interband transition also sits at this range. The dephasing of SP due to electron-phonon scattering can be merged into the frame of Lorentz-Drude model. The bandwidth and oscillator strengths of ω_{LSP} should be in similar order to the interband transitions. Intuitively, the oscillator strength f_{LSP} should be in positive correlation with the temperature, and is key to the amplitude modulation of nonlinear scattering. Experimental evidence suggested that temperature higher than room temperature to be a required for increasing electron-phonon scattering rate [57]. Hence, we assume f_{LSP} to be negligible at room temperature and increases with the temperature.

Here is the remark: the evaluation of electron-phonon scattering requires calculation of thermal energy with lattice temperature. In the previous sections, we validated the hot lattice mechanism to be dominant in nonlinear scattering, but how it dominates remains a mystery. In addition, the time scale of hot lattice dynamics (~100 ps, given in Table 2) is way too slow to be considered in Lorentz-Drude model. With new evidence [11], we can say that hot lattice facilitates the SP dephasing process through the increase in electron-phonon scattering rate.

In a typical Drude model, Γ_D (or Γ_0 in Lorentz-Drude model) increases with temperature due to the change in effective electron mass. Such process often called Drude broadening is experimentally derive to be 0.1meV per kelvin. In addition to Γ_D, other damping rate changes with temperature, too. In order to fit the result of measurement of

doi:10.6342/NTU201602833

bulk gold and calculation based on such result, the variation of ε_2 and ε_1 per kelvin are assumed to be +0.06% and -0.01%. With Eq. (38) and (39), the Lorentz-Drude parameters are corrected with temperature. Unfortunately, the formulation of temperature-dependent f_m is very difficult since it involves the modification to band structures in system way complex than free-electron systems [58]. The variation in f_m also couples with the variation in ω_m. As a phenomenological model, the variation of ω_m and Γ_m are sufficient to provide satisfactory fitting as demonstrated in Figure 19.

In Figure 19(a), we simulate the bulk permittivity changing with temperature, and the permittivity does not change obviously (6% in imaginary part, 1% in real part as stated in previous paragraph). In Figure 19(b), from 300 to 400K, the scattering intensity decreases for 10%, and the resonance slightly blueshifts.

In Figure 20 (a), with the LSP oscillator added at ω_{LSP}, the imaginary significantly increases at the LSPR. Also, ω_{LSP} gives a similar oscillator bandwidth (500-700nm) as Figure 18, which is in consistent with selection of the damping rate. In Figure 20(b), the scattering intensity decreases for 70% (with the background subtracted).

doi:10.6342/NTU201602833

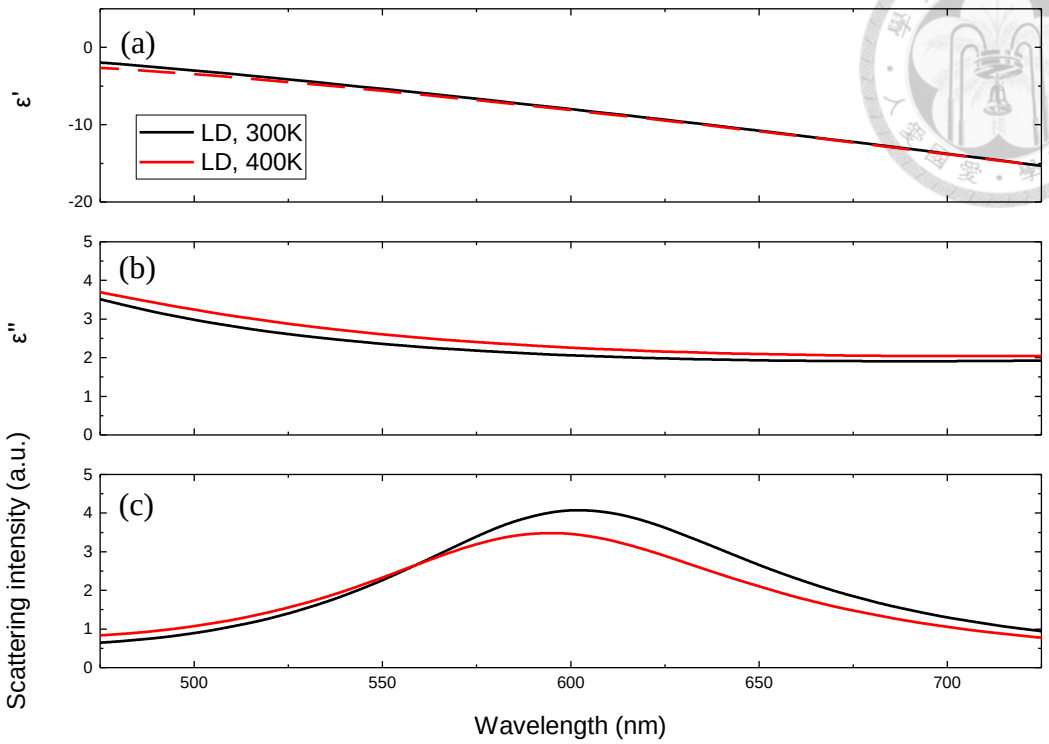

Figure 19. (a) The real part ε' and (b) imaginary part ε'' of permittivity calculated by Lorentz-Drude model without LSP damping. (c) The calculated Mie scattering efficiency from (a) and (b).

doi:10.6342/NTU201602833

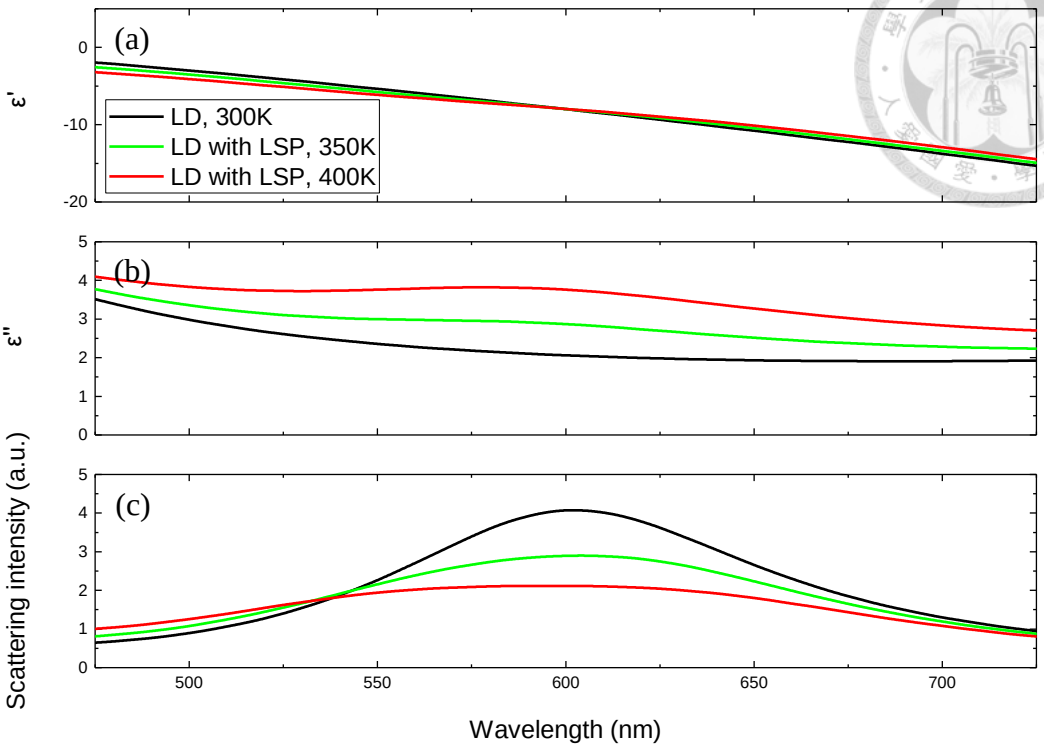

Figure 20. (a) The real part ε' and (b) imaginary part ε'' of permittivity calculated by Lorentz-Drude model with LSP damping. (c) The calculated Mie scattering efficiency from (a) and (b).

Temperature (K)	300	350	400
f_{LSP}	0	0.01	0.025
Γ_{LSP} (eV)	--	0.55	0.65

Table 4 The fitting parameters of LSP damping in Figure 20.

4.4 Discussion

4.4.1 The applicability of the LSP damping model and further developments

In 4.3, the model relies solely on modification of the dielectric function. For an

doi:10.6342/NTU201602833

arbitrary system, Mie theory can be replaced with finite-difference time-domain (FDTD). Hence, as long as the LSPR of the system is given, the LSP damping model should be compatible with system of any geometry.

The model is directly linked to the physical process of LSP damping. Though the description of the process should be correct, the fitting could be more polished. The exact total damping rate can be extracted from measuring the bandwidth of the scattering spectra. In addition, the total damping rate should also be decoupled into various mechanisms, including electron-electron, electron-phonon scattering and other macroscopic effects [10, 11]. The electron-phonon scattering rate is the most important term when it comes to thermal effect. Above the Debye temperature, the electron-phonon scattering rate is proportional to thermal energy and temperature (of the lattice) [11]:

$$\frac{1}{\tau_{e-ph}} \sim E_{thermal} \sim AT \,, \tag{54}$$

where A is a constant proportional to specific heat. One may also want to work out an intensity-dependent model. To do so, the thermal energy of the nanoparticle under laser excitation has to be evaluated [28].

The oscillator strength can either be described quantum mechanically [58], or with Bose-Einstein harmonic oscillator [45]. With all the parameters corrected, the physics of saturable scattering would be fully uncovered, and the accuracy of the model should be significantly improved.

4.4.2 Possible mechanism for reverse saturable scattering

Saturable scattering can be easily foreseen through the increasing imaginary part of permittivity and the damping of LSP. In our measurement [33] and Shalaev *et al* [45] with temperature range up to 800K, the imaginary part of the permittivity mostly increases with the temperature. From room temperature to annealing temperature, the imaginary

doi:10.6342/NTU201602833

part of permittivity increases as the electron-phonon scattering rates increase. Around the annealing temperature, the imaginary part of permittivity slightly decreases as the mean free path increases due to merging of grains. Beyond 650K, the imaginary part significantly increases because of the development of pores on the surface of gold. Nevertheless, to achieve reverse saturable scattering, the imaginary part should be significantly decreases. This violates everything happens in bulk gold as the temperature increases.

If reverse saturation has a similar mechanism to saturation, one shall see reverse saturation in both optically excitation and environmental heating. For optically excitation, reverse saturable absorption in gold nanorods in solution is observed by Elim *et al*[59] in and, more recently, by Baldovino-Pantaleón *et al* [60]. For environmental heating, Yeshchenko *et al* [10] have the data of highest temperature (~1200K) ever reported. From 300 to 1200K, the sign of reverse saturable scattering is not observed. Surprisingly, the reported reverse saturation are all in aqueous environment under optical excitation. There are several possibilities when reverse saturation occurs: i) particle deformation [59], ii) nanobubbles [61], and iii) the electron population redistribution due to Fermi smearing [9]. The first one can be verified with reproducibility test, while the second can be measured with photoacoustic imaging. The last one is recently predicted by theoretical calculations.

doi:10.6342/NTU201602833

Chapter 5 Conclusion

In this thesis, we confirm the mechanism of nonlinear scattering to be hot lattice by extracting its nonlinear refractive index from intensity dependence test. The spectral single particle modulation experiments show that the amplitude of LSPR significantly weakens, but not shift obviously. In addition, such nonlinear behavior should be found in other materials as long as their permittivity changes with temperature. The new nonlinearity opens up a new dimension for hot lattice material in plasmonics. Nevertheless, conventional Mie theory cannot explain such large nonlinearity. We adapt Maxwell-Garnett theory and find the single-particle nonlinearity amplified around LSPR. The result also shows the importance of ambient medium since its temperature dependence further boost the quantity of nonlinearity. Finally, the hints from Maxwell-Garnett theory enlighten us that nanoparticles should have a very different permittivity. We add an innovative correction term to the Lorentz-Drude model to describe such anomaly. With the new Lorentz-Drude parameters, the actual physical process of nonlinear scattering, and the role of hot lattice are revealed. However, the model is limited to saturable scattering. The reverse saturable scattering should rely on other mechanisms.

doi:10.6342/NTU201602833

REFERENCE

1. D. Pines, and D. Bohm, "A collective description of electron interactions: II. collective vs individual particle aspects of the interactions," Phys. Rev. **85**, 338-353 (1952).
2. W. Nie, "Optical nonlinearity: phenomena, applications, and materials," Adv. Mater. **5**, 520-545 (1993).
3. M. Kauranen, and A. V. Zayats, "Nonlinear plasmonics," Nature Photon. **6**, 737-748 (2012).
4. Y. Chen, and H. Ming, "Review of surface plasmon resonance and localized surface plasmon resonance sensor," Photonic Sensors **2**, 37-49 (2012).
5. R. P. H. Kooyman, R. M. Corn, A. Wark, H. J. Lee, E. Gedig, G. Engbers, L. Walstrom, N. J. de Mol, D. R. Hall, P. Yager, T. Chinowsky, E. Fu, K. Nelson, A. McWhirter, M. J. E. Fischer, A. M. C. Lokate, J. B. Beusink, G. J. M. Pruijn, W. Knoll, A. Kasry, J. Liu, T. Neumann, L. Niu, H. Park, H. Paulsen, R. Robelek, F. Yu, and P. Schuck, *Handbook of surface plasmon resonance* (The Royal Society of Chemistry, 2008).
6. J. Bigot, J. Merle, O. Cregut, and A. Daunois, "Electron dynamics in copper metallic nanoparticles probed with femtosecond optical pulses," Phys. Rev. Lett. **75**, 4702-4705 (1995).
7. S. Link, and M. A. El-Sayed, "Shape and size dependence of radiative, non-radiative and photothermal properties of gold nanocrystals," Int. Rev. Phys. Chem. **19**, 409-453 (2000).
8. L. Sarkhosh, and N. Mansour, "Study of the solution thermal conductivity effect on nonlinear refraction of colloidal gold nanoparticles," Laser Phys. **25**, 065404 (2015).
9. Y. Sivan, and S.-W. Chu, "Nonlinear plasmonics at high temperatures," in *ArXiv e-prints*(2016).
10. O. A. Yeshchenko, I. S. Bondarchuk, V. S. Gurin, I. M. Dmitruk, and A. V. Kotko, "Temperature dependence of the surface plasmon resonance in gold nanoparticles," Surf. Sci. **608**, 275-281 (2013).
11. Q.-C. Sun, Y. Ding, S. M. Goodman, H. H. Funke, and P. Nagpal, "Copper plasmonics and catalysis: role of electron-phonon interactions in dephasing localized surface plasmons," Nanoscale **6**, 12450-12457 (2014).
12. Y. Guillet, M. Rashidi-Huyeh, D. Prot, and B. Palpant, "Gold nanoparticle assemblies: interplay between thermal effects and optical response," Gold Bull **41**, 341-348 (2008).
13. V. P. Zharov, and D. O. Lapotko, "Photothermal imaging of nanoparticles and cells," IEEE J. Sel. Top. Quantum Electron. **11**, 733-751 (2005).
14. X. Huang, P. K. Jain, I. H. El-Sayed, and M. A. El-Sayed, "Plasmonic photothermal therapy (PPTT) using gold nanoparticles," Lasers Med Sci **23**, 217-228 (2008).
15. Y. Sonnefraud, H. G. Sinclair, Y. Sivan, M. R. Foreman, C. W. Dunsby, M. A. A. Neil, P. M. French, and S. A. Maier, "Experimental proof of concept of nanoparticle-assisted STED," Nano Lett. **14**, 4449-4453 (2014).
16. S.-W. Chu, T.-Y. Su, R. Oketani, Y.-T. Huang, H.-Y. Wu, Y. Yonemaru, M. Yamanaka, H. Lee, G.-Y. Zhuo, M.-Y. Lee, S. Kawata, and K. Fujita, "Measurement of a saturated emission of optical radiation from gold nanoparticles: Application to an ultrahigh resolution microscope," Phys. Rev. Lett. **112**, 017402 (2014).
17. S. Molesky, C. J. Dewalt, and Z. Jacob, "High temperature epsilon-near-zero and epsilon-near-pole metamaterial emitters for thermophotovoltaics," Opt. Express **21**, A96-

doi:10.6342/NTU201602833

A110 (2013).
18. X. Chen, A. Munjiza, K. Zhang, and D. Wen, "Molecular dynamics simulation of heat transfer from a gold nanoparticle to a water pool," J. Phys. Chem. C **118**, 1285 - 1293 (2014).
19. Z. Fang, Y. R. Zhen, O. Neumann, A. Polman, F. J. G. de Abajo, P. Nordlander, and N. J. Halas, "Evolution of light-induced vapor generation at a liquid-immersed metallic nanoparticle," Nano Lett. **13**, 1736-1742 (2013).
20. W. L. Barnes, "Metallic metamaterials and plasmonics," Philos. Transact. A **369**, 3431-3433 (2011).
21. D. Kraemer, B. Poudel, H.-P. Feng, J. C. Caylor, B. Yu, X. Yan, Y. Ma, X. Wang, D. Wang, A. Muto, K. McEnaney, M. Chiesa, Z. Ren, and G. Chen, "High-performance flat-panel solar thermoelectric generators with high thermal concentration," Nat. Mater. **10**, 532-538 (2011).
22. C. Clavero, "Plasmon-induced hot-electron generation at nanoparticle/metal-oxide interfaces for photovoltaic and photocatalytic devices," Nature Photon. **8**, 95-103 (2014).
23. D. A. Boyd, L. Greengard, M. Brongersma, M. Y. El-Naggar, and D. G. Goodwin, "Plasmon-assisted chemical vapor deposition," Nano Lett. **6**, 2592-2597 (2006).
24. N. Zhou, X. F. Xu, A. T. Hammack, B. C. Stipe, K. Z. Gao, W. Scholz, and E. C. Gage, "Plasmonic near-field transducer for heat-assisted magnetic recording," Nanophotonics **3**, 141-155 (2014).
25. S.-W. Chu, H.-Y. Wu, Y.-T. Huang, T.-Y. Su, H. Lee, Y. Yonemaru, M. Yamanaka, R. Oketani, S. Kawata, S. Shoji, and K. Fujita, "Saturation and reverse saturation of scattering in a single plasmonic nanoparticle," ACS Photonics **1**, 32-37 (2014).
26. D. D. Smith, G. Fischer, R. W. Boyd, and D. A. Gregory, "Cancellation of photoinduced absorption in metal nanoparticle composites through a counterintuitive consequence of local field effects," J. Opt. Soc. Am. B **14**, 1625-1631 (1997).
27. H.-Y. Wu, Y.-T. Huang, P.-T. Shen, H. Lee, R. Oketani, Y. Yonemaru, M. Yamanaka, S. Shoji, K.-H. Lin, C.-W. Chang, S. Kawata, K. Fujita, and S.-W. Chu, "Ultrasmall all-optical plasmonic switch and its application to superresolution imaging," Sci. Rep. **6**, 24293 (2016).
28. Y.-T. Huang, "Mechanism of Nolinear Scattering of Single Gold Nanosphere," in *Department of Physics*(National Taiwan University, Taiwan, 2014).
29. S. Link, and M. A. El-Sayed, "Size and temperature dependence of the plasmon absorption of colloidal gold nanoparticles," J. Phys. Chem. B **103**, 4212-4217 (1999).
30. H. R. Moon, D.-W. Lim, and M. P. Suh, "Fabrication of metal nanoparticles in metal-organic frameworks," Chem. Soc. Rev. **42**, 1807-1824 (2013).
31. X. C. Li, J. M. Zhao, L. H. Liu, and J. Y. Tan, "Optical properties of edible oils within spectral range from 300 to 2500nm determined by double optical pathlength transmission method," Appl. Opt. **54**, 3886-3893 (2015).
32. S. A. Khodier, "Refractive index of standard oils as a function of wavelength and temperature," Opt. Laser Technol. **34**, 125-128 (2002).
33. P.-T. Shen, Y. Sivan, C.-W. Lin, H.-L. Liu, C.-W. Chang, and S.-W. Chu, "Temperature- and -roughness dependent permittivity of annealed/unannealed gold films," Opt. Express **24**, 19254-19263 (2016).
34. C. F. Bohren, and D. R. Huffman, "Absorption and scattering by a sphere," in *Absorption and scattering of light by small particles*(Wiley-VCH Verlag GmbH, 2007), pp. 82-129.
35. R. W. Boyd, "The intensity-dependent refractive index," in *Nonlinear Optics (Third Edition)*(Academic Press, Burlington, 2008), pp. 207-252.

doi:10.6342/NTU201602833

36. R. W. Boyd, "The nonlinear optical susceptibility," in *Nonlinear Optics (Third Edition)*(Academic Press, Burlington, 2008), pp. 1-67.
37. T. Stoll, P. Maioli, A. Crut, N. Del Fatti, and F. Vallée, "Advances in femto-nano-optics: ultrafast nonlinearity of metal nanoparticles," Eur. Phys. J. B **87**, 1-19 (2014).
38. F. Hache, D. Ricard, C. Flytzanis, and U. Kreibig, "The optical Kerr effect in small metal particles and metal colloids: the case of gold," Appl. Phys. A **47**, 347-357 (1988).
39. R. W. Boyd, Z. Shi, and I. De Leon, "The third-order nonlinear optical susceptibility of gold," Optics Communications **326**, 74-79 (2014).
40. H. S. Nalwa, "Organic materials for third-order nonlinear optics," Advanced Materials **5**, 341-358 (1993).
41. A. F. Jaffar, A. M. Salman, I. N. Akram, and A. A. A. Dergazly, "Nonlinear properties and optical limiting of olive oil by using z-scan technique," in *2012 First National Conference for Engineering Sciences (FNCES)*(IEEE, Baghdad, Iraq, 2012).
42. V. Liberman, M. Sworin, R. P. Kingsborough, G. P. Geurtsen, and M. Rothschild, "Nonlinear bleaching, absorption, and scattering of 532-nm-irradiated plasmonic nanoparticles," Journal of Applied Physics **113**, 053107 (2013).
43. R. C. Rumpf, "Electromagnetic properties of materials -part 1: Lorentz and Drude Models," in *21st Century Electromagnetics*(The University of Texas at El Paso).
44. F. Vallée, "Optical properties of metallic nanoparticles," in *Nanomaterials and Nanochemistry*, C. Bréchignac, P. Houdy, and M. Lahmani, eds. (Springer Berlin Heidelberg, Berlin, Heidelberg, 2007), pp. 197-227.
45. H. Reddy, U. Guler, A. V. Kildishev, A. Boltasseva, and V. M. Shalaev, "Temperature-dependent optical properties of gold thin films," in *ArXiv e-prints*(2016).
46. C. Mätzler, "MATLAB functions for Mie scattering and absorption," U. o. B. Institute of Applied Physics, ed. (2002).
47. M. Rashidi-Huyeh, and B. Palpant, "Counterintuitive thermo-optical response of metal-dielectric nanocomposite materials as a result of local electromagnetic field enhancement," Phys. Rev. B **74**, 075405 (2006).
48. V. Švorčík, J. Siegel, P. Šutta, J. Mistrík, P. Janíček, P. Worsch, and Z. Kolská, "Annealing of gold nanostructures sputtered on glass substrate," Appl. Phys. A **102**, 605-610 (2010).
49. T. Tanaka, "Immersion oil composition having low fluorescence emissions for microscope," (1988).
50. H. Lee, K.-Y. Li, Y.-T. Huang, P.-T. Shen, G. Deka, R. Oketani, Y. Yonemaru, M. Yamanaka, K. Fujita, and S.-W. Chu, "Measurement of scattering nonlinearities from a single plasmonic nanoparticle," e53338 (2016).
51. P. B. Johnson, and R. W. Christy, "Optical constants of noble metals," Phys. Rev. B **6**, 4370-4379 (1972).
52. G. P. Pells, and M. Shiga, "The optical properties of copper and gold as a function of temperature," J. Phys. C **2**, 1835 (1969).
53. M.-C. L. Yu-Jen Chen, Chih-Ming Wang, "Dielectric function dependence on temperature for Noble metal," in *18th Microoptics Conference (MOC'13)*(JSAP, Tokyo, Japan, 2013).
54. R. B. Wilson, B. A. Apgar, L. W. Martin, and D. G. Cahill, "Thermoreflectance of metal transducers for optical pump-probe studies of thermal properties," Opt. Express **20**, 28829 - 28838 (2012).
55. R. M. Christian Karnutsch, and Benjamin J. Eggleton, "Making temperature-insensitive optofluidic photonic-crystal devices," (SPIE, 2009), http://spie.org/newsroom/1706-making-temperature-insensitive-optofluidic-photonic-

doi:10.6342/NTU201602833

crystal-devices.
56. A. D. Rakić, A. B. Djurišić, J. M. Elazar, and M. L. Majewski, "Optical properties of metallic films for vertical-cavity optoelectronic devices," Appl. Opt. **37**, 5271-5283 (1998).
57. A. Giri, J. T. Gaskins, B. M. Foley, R. Cheaito, and P. E. Hopkins, "Experimental evidence of excited electron number density and temperature effects on electron-phonon coupling in gold films," J. Appl. Phys. **117**, 044305 (2015).
58. D. B. Tanner, "Optical effects in solids," (Department of Physics, University of Florida).
59. H. I. Elim, J. Yang, J.-Y. Lee, J. Mi, and W. Ji, "Observation of saturable and reverse-saturable absorption at longitudinal surface plasmon resonance in gold nanorods," Appl. Phys. Lett. **88**, 083107 (2006).
60. E. V. Garcia-Ramirez, S. Almaguer-Valenzuela, O. Sanchez-Dena, O. Baldovino-Pantaleon, and J. A. Reyes-Esqueda, "Third-order nonlinear optical properties of colloidal Au nanorods systems: saturable and reverse-saturable absorption," Opt. Express **24**, A154-A167 (2016).
61. G. Baffou, J. Polleux, H. Rigneault, and S. Monneret, "Super-heating and micro-bubble generation around plasmonic nanoparticles under CW illumination," J. Phys. Chem. C **118**, 4890-4898 (2014).

doi:10.6342/NTU201602833